The Astrophysical Journal, 704:975–988, 2009 October 20 doi:10.1088/0004-637X/704/2/975


# ROTATIONAL VELOCITIES FOR M DWARFS*

J. S. Jenkins[1,2], L. W. Ramsey[1], H. R. A. Jones[3], Y. Pavlenko[3], J. Gallardo[2], J. R. Barnes[3], and D. J. Pinfield[3]
[1] Department of Astronomy and Astrophysics, Pennsylvania State University, University Park, PA 16802, USA; jjenkins@astro.psu.edu
[2] Department of Astronomy, Universidad de Chile, Casilla Postal 36D, Santiago, Chile
[3] Center for Astrophysics, University of Hertfordshire, College Lane Campus, Hatfield, Hertfordshire AL10 9AB, UK
*Received 2009 January 9; accepted 2009 September 3; published 2009 September 25*

## ABSTRACT

We present spectroscopic rotation velocities ($v \sin i$) for 56 M dwarf stars using high-resolution Hobby–Eberly Telescope High Resolution Spectrograph red spectroscopy. In addition, we have also determined photometric effective temperatures, masses, and metallicities ([Fe/H]) for some stars observed here and in the literature where we could acquire accurate parallax measurements and relevant photometry. We have increased the number of known $v \sin i$ values for mid M stars by around 80% and can confirm a weakly increasing rotation velocity with decreasing effective temperature. Our sample of $v \sin i$s peak at low velocities (∼3 km s$^{-1}$). We find a change in the rotational velocity distribution between early M and late M stars, which is likely due to the changing field topology between partially and fully convective stars. There is also a possible further change in the rotational distribution toward the late M dwarfs where dust begins to play a role in the stellar atmospheres. We also link $v \sin i$ to age and show how it can be used to provide mid-M star age limits. When all literature velocities for M dwarfs are added to our sample, there are 198 with $v \sin i \leqslant 10$ km s$^{-1}$ and 124 in the mid-to-late M star regime (M3.0–M9.5) where measuring precision optical radial velocities is difficult. In addition, we also search the spectra for any significant H$\alpha$ emission or absorption. Forty three percent were found to exhibit such emission and could represent young, active objects with high levels of radial-velocity noise. We acquired two epochs of spectra for the star GJ1253 spread by almost one month and the H$\alpha$ profile changed from showing no clear signs of emission, to exhibiting a clear emission peak. Four stars in our sample appear to be low-mass binaries (GJ1080, GJ3129, Gl802, and LHS3080), with both GJ3129 and Gl802 exhibiting double H$\alpha$ emission features. The tables presented here will aid any future M star planet search target selection to extract stars with low $v \sin i$.

*Key words:* planetary systems – stars: fundamental parameters – stars: low-mass, brown dwarfs – stars: rotation

*Online-only material:* color figure

## 1. INTRODUCTION

In the past 10 yr radial-velocity measurements in the optical have made great strides by utilizing a number of techniques and methodologies to generate precisions of 3 m s$^{-1}$ in the long term (e.g., Butler et al. 2006) and sub-m s$^{-1}$ in the short term (e.g., Bouchy et al. 2005). Use of an iodine cell (e.g., Marcy & Butler 1992) or ThAr gas lamp (e.g., Pepe et al. 2000) has allowed detection of around 300 extrasolar planets (exoplanets), with that number increasing each month (see http://exoplanet.eu/). A large parameter space has been studied, but since these observations are limited to the optical regime, where M dwarfs are intrinsically faint, a vast amount of stars are left unobserved, particularly the M star population that constitutes the bulk of stars in the local galactic neighborhood. Radial-velocity studies of early M dwarfs have detected planets well into the terrestrial-mass regime, down below 10 $M_\oplus$ (e.g., Rivera et al. 2005; Udry et al. 2007; Mayor et al. 2009). There is considerably improved mass contrast with such stars (amplitude of a given mass planet $\propto M_{\rm star}^{0.5}$) and obtaining precision radial velocities of these objects may enable Earth-mass planets to be detected in their habitable zones.

The largest uncertainty associated with precision radial-velocity measurements is that of stellar activity. The association between stellar activity and rotation velocity ($v \sin i$) is well established (Noyes et al. 1984), and measuring this parameter is an excellent proxy of the level of activity. For a fixed resolution, S/N, and calibration method, stars with higher rotational velocities have radial-velocity measurements with lower precision since the larger rotation serves to wash out the spectral features (Bouchy et al. 2001). Coupled to this, the combination of activity and rotation can cause false positives to appear in the data (e.g., Henry et al. 2002), but in general it serves to increase the level of jitter (Wright 2005). However, the rotation–activity connection has been shown to saturate quickly around M stars, occurring at ∼5 km s$^{-1}$ for M2 objects (Patten & Simon 1996). Since we are probing later M stars (⩾M3), where observations of various activity indicators have shown that the percentage of active stars will increase dramatically, up to ∼100% at M7 (Fleming et al. 2000; Mohanty et al. 2002), we are focused on selecting the slowest rotators within each spectral bin, in order to select the narrowest line profiles. An increase in radial-velocity uncertainty of around 3–4 times was found by Bouchy et al. when increasing the $v \sin i$ of stellar models from 1 to 10 km s$^{-1}$. The larger uncertainty arises due to the loss of spectral information in the stars with higher $v \sin i$, since the blending factor is increased within the stellar forest, to the detriment of the radial-velocity information.

Based on the above description any future precision radial-velocity planet search survey targeting cool M stars should have a fairly strict selection based on the rotational velocity of their sample stars, particularly when targeting Earth-mass planets in the habitable zones. For instance, a search employed using a PRVS-like instrument (Jones et al. 2008; Ramsey et al. 2008)

* Based on observations obtained with the Hobby-Eberly Telescope, which is a joint project of the University of Texas at Austin, the Pennsylvania State University, Stanford University, Ludwig-Maximilians-Universität München, and Georg-August-Universität Göttingen.

would focus on selecting the brightest M stars with rotational velocities in the sub-10 km s$^{-1}$ regime, which would allow high S/N spectra to be acquired in the shortest possible observational times, gaining in the number of M stars observed in a single observing run, and also allowing the highest precisions to be reached to detect the lowest mass rocky planets, in particular Earth-like planets in their habitable zones. We do note that such a 10 km s$^{-1}$ upper limit should probably be raised when moving into the ultracool/brown dwarf regime to increase the number of such objects on any planet search sample since previous studies have shown that rotation velocities appear to systematically increase (e.g., Mohanty & Basri 2003; Reiners & Basri 2008).

## 2. OBSERVATIONS & REDUCTION

All observations in this study were made over the period 2006 December 25–2007 November 4 utilizing the queue scheduling mode at the 9.2 m Hobby–Eberly Telescope (HET; Ramsey et al. 1998) at McDonald Observatory in Texas. Using the High Resolution Spectrograph (HRS; Tull 1998) red chip (∼8100–9900 Å) operating at a resolution of $R \sim 37{,}000$ and spatial binning of 2 × 2, 53 objects were observed, ranging in spectral type from M3V to M6.5V. The HRS observing mode employed the use of two 3″ fibers since the objects were so faint, with one on object and one on sky. Bright telluric standards taken from the HET list of rapidly rotating B stars were also observed on most of the nights, which allowed us to characterize the level of telluric contamination in the data. Since even close by mid-to-late M stars are relatively faint, our HRS integration times ranged in duration from 5–25 minutes and for some of the fainter objects multiple exposures were taken and combined to generate a high S/N spectrum. However, most of the $v \sin i$ measurements, when comparing the individual frames to the combined frame, were within ±0.5 km s$^{-1}$ since the deconvolution method we employ boosts the S/N in the final line profile used in the measurements.

The reduction of all data was performed using CCDPACK and STARLINK techniques. First the bias and overscan signals were removed and the overscan region was clipped off each image. A master flat field was created by median filtering all flats taken in the standard HRS calibration plan. This usually consisted of a few bias frames, flat fields, and ThAr arc observations taken before and after the nights observing; however, for one night no flats were observed and a flat field from a night close to the observing night was used in the reduction. Also the number of flat fields was increased to 10 for the last six months or so of data, which significantly aids in fringe removal. Indeed, the fringing in the red chip of HRS can reach 10%–20% and hence well-exposed, high S/N Halogen flat fields are used to correct these.

The STARLINK package ECHOMOP (Mills et al. 1996) was used to extract the echelle data. First, all 14 orders were located and traced using the master flat field, and any stray pixels were clipped from this trace. The dekker limits were determined using the master flat field to ensure that the entire object order and the adjoining sky order are included in the reduction. The master flat field was then normalized to determine the balance factors, and these were multiplied into all other observations. The skylight was removed by utilizing the sky fiber and subtracting out any skylines that appeared in the object spectra. The orders were then extracted using an optimal extraction routine (Horne 1986) and wavelength calibrated using the ThAr arc images.

A small portion of spectra for the M4.5V star G 121−028, centered on the sodium doublet at 8182–8194 Å, is shown in Figure 1(solid line). The dashed spectrum is the telluric standard HD1839, which is a fast rotating B star; therefore, all the strong features are due to telluric contamination. The sodium doublet is heavily blended with a number of telluric features, which without good sky subtraction, could serve to contaminate any measurement of the line properties. This is one of the reasons that we use a spectral deconvolution routine to help remove the telluric features in our final analysis. These final spectra have a limiting resolution of between ∼0.20 and 0.35 Å (∼7–13 km s$^{-1}$), which was determined individually for each star by deconvolving the telluric lines in each image.

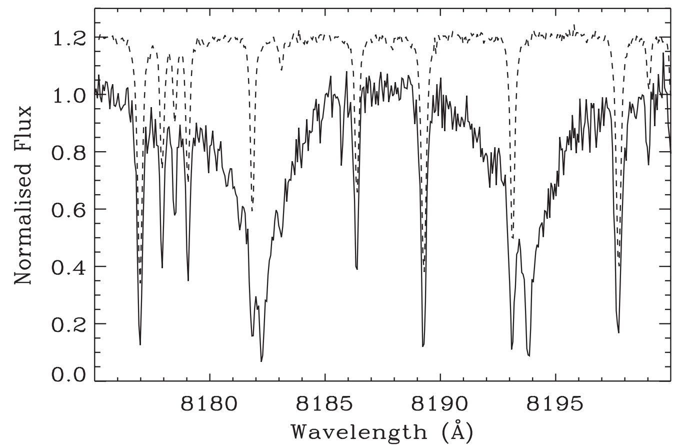


**Figure 1.** Normalized HRS spectra for the M4.5 dwarf G 121−028 around the sodium doublet (8182–8194 Å) is shown by the solid line. The dashed line represents the telluric standard HD1839 and has been offset for clarity. Note the blending between the strong sodium lines and the tellurics in the M dwarf spectra.

## 3. $v \sin i$ DETERMINATION

All $v \sin i$s in this work are determined by deriving an optimal line profile for each star, and then convolving a non-rotating template (LHS1950 is our template) with rotational profiles of various velocities to find the best match. A deconvolution method (Donati & Collier Cameron 1997; Barnes et al. 1998; Collier Cameron et al. 2002) is used to determine the optimal line profile. A continuum fit is performed using the CONTINUUM routine in IRAF to normalize the spectra and to provide inverse variance weights for the deconvolution procedure. This least-squares deconvolution uses a line list which best matches the spectral type of each star. The wavelength positions and line depths used were taken from Vienna Atomic Line Database (VALD; Kupka & Ryabchikova 1999). Any deficiencies in the line list data for cool M stars, such as missing opacities, should not affect the final $v \sin i$ values, since the same list is used on the non-rotating template star LHS1950. The use of fewer model lines for deconvolution than actually observed will simply give rise to profiles with lower S/N than a more complete model would afford. The line strengths of the final profiles may also vary from star to star but can be corrected for by scaling the non-rotating template to the line strength of each stellar deconvolved profile. The method of least-squares deconvolution is used to determine the mean line profile which when convolved with the line depth pattern gives the optimal match to the observed spectrum.

Figure 2 represents the final deconvolved line profile for G 121−028 (solid line) with velocity on the $x$-axis and normalized flux on the $y$-axis. G 121−028 is one of the slower rotating stars in our sample ($v \sin i = 3.8 \pm 0.7$ km s$^{-1}$) as the narrow line profile shows. To determine the $v \sin i$ values,

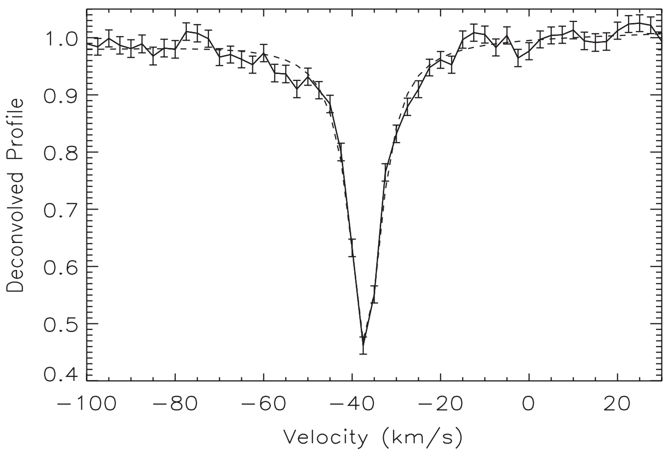


**Figure 2.** Deconvolved line profile for the star G 121−028 in velocity space (vacuum velocities). The best fit to this profile is marked by the dashed line.

we perform a Levenberg–Marquardt least-squares minimization using MPFIT in IDL (Markwardt 2009) to find the best fit for each observed line profile. The fit is represented by the dashed line in the figure and for this example a reduced $\chi^2$ ($\chi^2_\nu$) of 1.2 is found. This best fit is used to determine both the profile centroid and scaling factor. The centroid allows each star to be shifted to the rest frame for use in the template comparison, whilst the scaling factor allows us to scale our non-rotating template to match the profile strength of each star. LHS1950 was found to be our narrowest profile (determined from the full width at half maximum, FWHM, of the best fit to each profile) and hence below the resolution limit of the instrument. This template is then broadened in steps of 0.5 km s$^{-1}$, between velocities of 0.5 and 50 km s$^{-1}$, using a grid of rotational profiles with a limb-darkening coefficient of 0.6. An example is shown in Figure 3. A zoomed in the region of the profile of G 121−028 is represented by the dotted curve, with template profiles marked by the solid curves. From inner to outer (narrowest to broadest), the solid curves have been broadened by rotational profiles of 3.5, 5.0, and 10.0 km s$^{-1}$, respectively. This highlights the good fit between the inner profile compared to the outer profiles within the uncertainties and highlights the robust nature of the fitting technique. All rotational profiles are generated following the description in Gray (1992), and a $\chi^2$ value is determined at each $v$ sin $i$ step.

Figure 4 shows our $\chi^2$ fit to the data points in the analysis of the star G 180−011. Each filled circle represents one of the 0.5 km s$^{-1}$ steps used to broaden the template to fit the profile of G 180−011. The solid curve represents the best quadratic fit to the data, and following the procedure in Jenkins et al. (2008), the minimum of this curve is the measured $v$ sin $i$, highlighted here by the vertical solid line. The vertical dotted, dot-dashed, and dashed lines represent the 1$\sigma$, 2$\sigma$, and 3$\sigma$ internal uncertainties, respectively. The 1$\sigma$ uncertainty value was determined by measuring the width of the curve at a 1$\sigma$ step (i.e., $\chi^2_{1\sigma} = \chi^2_{\rm min} + 1$), after the curve has been broadened by a factor determined from the difference between the minimum of the $\chi^2_\nu$ and 1 (where $\chi^2_\nu$ is the best fit). Due to the nature of the data set, this factor has a median of only 2.1 and standard deviation of 1.5, indicating the goodness of the methodology. We employ this artificial broadening to the $\chi^2$ curve to help alleviate uncertainties that are difficult to address in the analysis procedure e.g., macroturbulence variations, spectral-type differences, etc. For G 180−011 shown in the figure the formal uncertainty is found to be ±0.4 km s$^{-1}$. We use this procedure to determine all 1$\sigma$ uncertainties quoted in Table 1.

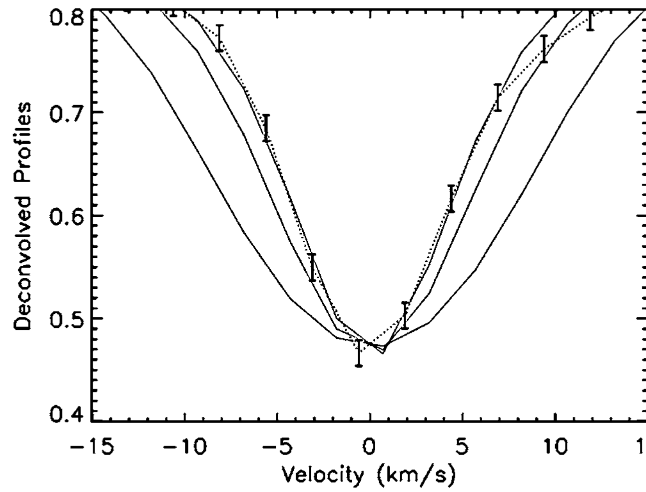


**Figure 3.** Zoomed-in region of the deconvolved profile of G 121−028 (dotted curve), along with three broadened template profiles (solid curves). From inner to outer the template has been broadened by velocities of 3.5, 5.0, and 10.0 km s$^{-1}$, respectively.

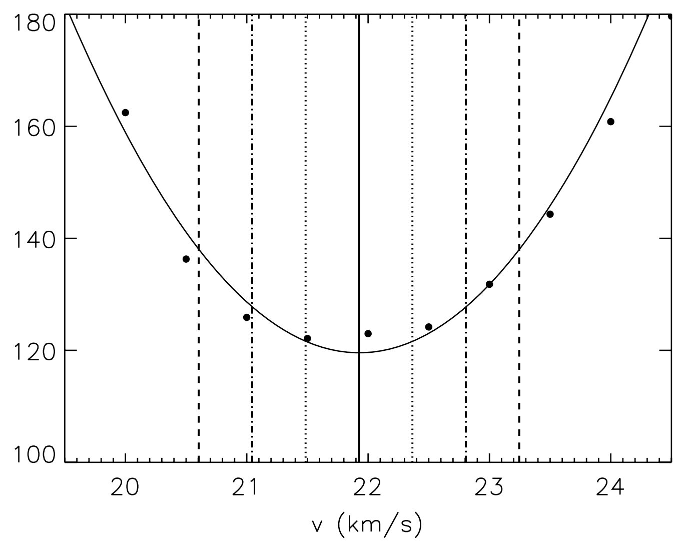


**Figure 4.** Subsection of the best-fit $\chi^2$ curve to the data (filled circles) for the star G 180−011. The solid curve marks the best fit, with the minimum of this function marked by the vertical solid line. The observed rotational velocity is 21.9 km s$^{-1}$ for this star. The dotted, dot-dashed, and dashed lines mark the determined 1$\sigma$, 2$\sigma$, and 3$\sigma$ limits, respectively.

The 1$\sigma$ uncertainties mentioned show that we have good internal precision and since we have a few stars where multiple observations were taken we can test this in a brute force manner by looking at the values for these multiple measurements individually. When we do this, we find that the $v$ sin $i$s tend to agree to within the uncertainties determined by the $\chi^2$-fitting procedure on each individual measurement. This gives us confidence in the analysis procedure. We note that for the star GJ1253 the $v$ sin $i$ values agree to within 1$\sigma$, which for this star was ~1 km s$^{-1}$, and as these were measured over two observations a month apart, they are probably the best indicator of the overall random uncertainties in the analysis procedure. Therefore, all velocities for objects $\leqslant$10 km s$^{-1}$ are accurate to ±1 km s$^{-1}$. For the objects rotating much faster than this, particularly above 20 km s$^{-1}$, it is difficult to fit their profiles to better than ~±10%–20% at the adopted resolution and S/N,

**Table 1**
Characteristics of M Stars in This Study

| Star | $V$ | $J$ | $H$ | $K_s$ | Spec Type | $T_{EFF}$ (K) | $\pi$ (mas) | $M/M_\odot$ | [Fe/H]$_{phot}$ | $v \sin i$ (km s$^{-1}$) | FWHM$_{Tell}$ (km s$^{-1}$) | H$\alpha$ Emission |
|---|---|---|---|---|---|---|---|---|---|---|---|---|
| G121−028 | 14.57 | 9.94 | 9.31 | 9.02 | M4.5 | 2948 | 54.00 ± 8.00 | 0.200 ± 0.005 | ... | 3.8 ± 0.7 | 7.2 | No* |
| G180−011† | 13.68 | 8.93 | 8.26 | 8.04 | M4.5 | 2913 | 92.00 ± 14.00 | 0.184 ± 0.003 | ... | 21.9 ± 0.4 | 6.8 | Yes |
| GJ1029 | 14.81 | 9.49 | 8.88 | 8.55 | M5.0 | 2765 | 79.30 ± 3.00 | 0.158 ± 0.016 | ... | 4.1 ± 0.8 | 7.2 | No |
| GJ1034 | 15.05 | 10.70 | 10.17 | 9.91 | M4.0 | 3035 | 48.10 ± 4.50 | 0.166 ± 0.025 | ... | ⩽4.5 | 10.9 | No* |
| GJ1055 | 14.86 | 9.93 | 9.33 | 9.07 | M5.0 | 2863 | 83.90 ± 4.00 | 0.133 ± 0.010 | ... | 4.7 ± 0.7 | 7.5 | No |
| GJ1078 | 15.52 | 10.70 | 10.19 | 9.85 | M4.5 | 2893 | 48.00 ± 4.50 | 0.158 ± 0.006 | ... | 7.2 ± 0.9 | 7.6 | Yes |
| GJ1119 | 13.32 | 8.60 | 8.03 | 7.74 | M4.5 | 2922 | 96.90 ± 2.70 | 0.200 ± 0.006 | ... | 4.0 ± 0.7 | 6.8 | Yes |
| GJ1134 | 12.96 | 8.49 | 8.01 | 7.71 | M4.5 | 2996 | 96.70 ± 2.30 | 0.212 ± 0.007 | ... | 4.1 ± 0.7 | 7.1 | No* |
| GJ1182† | 14.30 | 9.43 | 8.94 | 8.62 | M5.0 | 2880 | 71.70 ± 3.40 | 0.180 ± 0.003 | ... | 6.8 ± 0.5 | 6.5 | No |
| GJ1186 | 15.29 | 10.58 | 9.97 | 9.65 | M4.5 | 2924 | 53.50 ± 4.10 | 0.157 ± 0.008 | ... | 3.9 ± 0.6 | 7.8 | No |
| GJ1187 | 15.52 | 10.21 | 9.64 | 9.27 | M5.5 | 2767 | 89.00 ± 4.60 | 0.114 ± 0.006 | ... | 13.6 ± 0.6 | 6.3 | Yes |
| GJ1223 | 14.89 | 9.72 | 9.19 | 8.89 | M5.0 | 2802 | 83.50 ± 3.90 | 0.139 ± 0.002 | ... | ⩽4.5 | 10.0 | No* |
| GJ1250 | 14.88 | 9.96 | 9.40 | 9.08 | M4.5 | 2727 | 46.80 ± 6.20 | 0.213 ± 0.023 | 0.03 | 15.7 ± 0.4 | 8.1 | Yes |
| GJ1253 | 14.04 | 9.03 | 8.48 | 8.10 | M5.0 | 2842 | 107.50 ± 3.60 | 0.152 ± 0.002 | ... | ⩽4.5 | 12.1 | No/Yes |
| GJ1268 | 14.94 | 10.16 | 9.60 | 9.30 | M4.5 | 2904 | 62.70 ± 3.60 | 0.157 ± 0.008 | ... | ⩽4.5 | 11.5 | No |
| GJ2045 | 15.28 | 10.21 | 9.69 | 9.37 | M5.0 | 2827 | ... | ... | ... | 4.6 ± 0.3 | 7.0 | No |
| GJ3028 | 16.09 | 10.28 | 9.69 | 9.33 | M5.5 | 2654 | 79.30 ± 3.70 | 0.115 ± 0.005 | ... | ⩽4.5 | 12.9 | No |
| GJ3104 | 12.83 | 9.14 | 8.52 | 8.28 | M3.0 | 3289 | 41.00 ± 3.00 | 0.386 ± 0.001 | −0.20 | 4.0 ± 0.3 | 7.6 | No* |
| GJ3128 | 15.61 | 9.84 | 9.25 | 8.93 | M6.0 | 2662 | 112.00 ± 3.20 | 0.105 ± 0.002 | ... | ⩽4.5 | 12.3 | No |
| GJ3147 | ... | 9.98 | 9.35 | 9.01 | M5.0 | 2380* | ... | ... | ... | 28.2 ± 0.7 | 11.1 | Yes |
| GJ3153 | 14.78 | 10.06 | 9.56 | 9.20 | M4.5 | 2922 | 41.00 ± 17.00 | 0.234 ± 0.021 | 0.00 | 23.3 ± 0.7 | 7.0 | Yes |
| GJ3172 | 15.16 | 10.55 | 9.97 | 9.69 | M4.0 | 2954 | 40.20 ± 4.30 | 0.200 ± 0.001 | ... | 4.9 ± 0.9 | 7.4 | Yes |
| GJ3181 | 16.86 | 10.97 | 10.52 | 10.19 | M6.0 | 2636 | 68.50 ± 3.50 | 0.100 ± 0.006 | ... | 6.2 ± 0.8 | 7.1 | No |
| GJ3225 | 14.96 | 10.12 | 9.52 | 9.25 | M4.5 | 2888 | 60.00 ± 9.00 | 0.164 ± 0.002 | ... | 21.9 ± 0.6 | 8.8 | Yes |
| GJ3234 | 16.67 | 12.05 | 11.54 | 11.26 | M5.0 | 2951 | 34.60 ± 4.70 | 0.129 ± 0.023 | ... | ⩽4.5 | 11.9 | No |
| GJ3311 | 16.45 | 11.56 | 11.06 | 10.76 | M6.0 | 2874 | 52.10 ± 0.90 | 0.110 ± 0.019 | ... | ⩽4.5 | 11.1 | No |
| GJ3396 | 14.83 | 9.68 | 9.12 | 8.81 | M5.0 | 2807 | 90.00 ± 15.00 | 0.134 ± 0.003 | ... | 39.6 ± 1.7 | 7.7 | Yes |
| GJ3421 | 13.30 | 8.54 | 8.09 | 7.78 | M5.0 | 2910 | 108.50 ± 2.10 | 0.180 ± 0.004 | ... | 4.7 ± 0.6 | 7.4 | No* |
| GJ3444† | 15.16 | 11.92 | 11.38 | 11.09 | M6.0 | 3519 ? | 55.00 ± 4.00 | 0.125 ± 0.057 | ... | ⩽4.5 | 10.3 | No |
| GJ3515 | 15.40 | 10.68 | 10.08 | 9.80 | M4.5 | 2922 | 46.00 ± 17.00 | 0.168 ± 0.005 | ... | 13.1 ± 0.7 | 7.2 | Yes |
| GJ4030 | 13.54 | 9.32 | 8.63 | 8.45 | M3.5 | 3079 | 44.80 ± 4.10 | 0.312 ± 0.020 | −0.04 | ⩽4.5 | 10.5 | No* |
| GJ4108 | 15.37 | 10.75 | 10.24 | 9.97 | M4.5 | 2951 | 47.30 ± 4.10 | 0.159 ± 0.016 | ... | ⩽4.5 | 10.6 | No |
| GJ4345† | 16.10 | 11.09 | 10.48 | 10.17 | M5.0 | 2842 | 41.60 ± 3.20 | 0.152 ± 0.001 | ... | 9.8 ± 1.1 | 6.9 | Yes |
| GJ4385 | 16.10 | 10.87 | 10.26 | 9.93 | M5.0 | 2787 | 51.90 ± 0.90 | 0.136 ± 0.002 | ... | ⩽4.5 | 12.0 | No |
| Gl359 | 14.20 | 9.63 | 9.09 | 8.81 | M4.5 | 2966 | 79.00 ± 3.80 | 0.162 ± 0.016 | ... | 3.2⩽1.1 | 7.0 | No |
| Gl585 | 13.68 | 9.11 | 8.62 | 8.30 | M4.5 | 2966 | 85.10 ± 2.90 | 0.184 ± 0.009 | ... | 3.1 ± 0.5 | 6.4 | No* |
| LHS252 | 15.05 | 9.61 | 9.00 | 8.67 | M5.5 | 2737 | 99.80 ± 3.40 | 0.126 ± 0.003 | ... | 4.0 ± 0.5 | 7.4 | Yes |
| LHS265 | 15.11 | 10.26 | 9.70 | 9.40 | M4.5 | 2885 | 64.40 ± 4.00 | 0.147 ± 0.008 | ... | 3.9 ± 0.8 | 7.4 | No |
| LHS302 | 15.14 | 10.29 | 9.74 | 9.46 | M5.0 | 2885 | 57.20 ± 3.70 | 0.158 ± 0.006 | ... | ⩽2.5 | 7.0 | No |
| LHS1785 | 14.54 | 10.04 | 9.51 | 9.18 | M4.5 | 2987 | 58.80 ± 1.90 | 0.180 ± 0.012 | ... | 4.5 ± 0.6 | 6.8 | No |
| LHS1809 | 14.48 | 9.35 | 8.77 | 8.44 | M5.0 | 2812 | 107.70 ± 2.60 | 0.133 ± 0.003 | ... | 4.3 ± 1.2 | 6.4 | No |
| LHS1857 | 14.22 | 9.79 | 9.31 | 8.99 | M4.5 | 3009 | 54.70 ± 2.40 | 0.209 ± 0.009 | ... | 4.0 ± 0.5 | 7.3 | No |
| LHS1950 | 14.75 | 9.97 | 9.40 | 9.09 | M4.5 | 2904 | 62.70 ± 3.10 | 0.169 ± 0.002 | ... | ⩽2.5 | 7.3 | No |
| LHS2090 | ... | 9.44 | 8.84 | 8.44 | M6.5 | 2753** | ... | ... | ... | 20.0 ± 0.6 | 6.7 | Yes |
| LHS2206 | 14.05 | 9.21 | 8.60 | 8.33 | M4.5 | 2888 | 108.39 ± 2.30 | 0.143 ± 0.009 | ... | 16.5 ± 0.4 | 7.1 | Yes |
| LHS2320 | 14.40 | 9.83 | 9.28 | 8.94 | M5.0 | 2966 | 46.00 ± 8.00 | 0.239 ± 0.016 | −0.03 | 19.1 ± 0.2 | 6.3 | Yes |
| LHS2930† | ... | 10.79 | 10.14 | 9.79 | M6.5 | 2906** ? | ... | ... | ... | 18.7 ± 1.5 | 8.2 | Yes |
| LHS3075 | 14.17 | 9.59 | 9.02 | 8.72 | M4.5 | 2963 | 51.10 ± 4.40 | 0.239 ± 0.015 | −0.04 | ⩽2.5 | 5.8 | No |
| LP205−49 | 18.71 | 14.70 | 14.19 | 13.90 | M3.5 | 3156 | ... | ... | ... | 45.4 ± 2.0 | 7.7 | Yes |

**Notes.** The † symbol relates to deconvolved profiles that show either weak evidence for a possible binary component, but not significant enough to be included in the binary table, however it may affect the deconvolved profile enough to give rise to a larger rotation velocity than the star has, or stars where the deconvoluted profile has low S/N and the construction is of lower quality, particularly in the wings, which again can give rise to an inaccurate value for the $v \sin i$. The question marks after the effective temperature are used to flag highly suspect values. The asterisks in the H$\alpha$ column represent stars with significant absorption. The uncertainties shown for the $v \sin i$ values represent the formal uncertainties on each parameter fit. However, as explained in the text, the actual uncertainties for high S/N spectra of objects rotating ⩽20 km s$^{-1}$ is ±1 km s$^{-1}$, increasing to around 10%–20% for the fastest rotating objects.

and therefore this should be taken as the accuracy for such fast rotators.

### 3.1. Instrumental Profile

Although we estimate our resolution limit to be around 2.5 km s$^{-1}$, we note that this is not the case for all of our sample. Since we use a fixed template spectrum that was measured on our first night and not on every night of our observations, there will be effects due to the changes of the instrumental response. To monitor this, we used the telluric lines in each of our spectra as a proxy for the instrumental profile (IP). We assume that the intrinsic width of weak telluric lines is smaller than the instrumental resolution. We then performed the same fitting routine to these deconvolved profiles which returned an instrumental FWHM for each stellar spectrum.

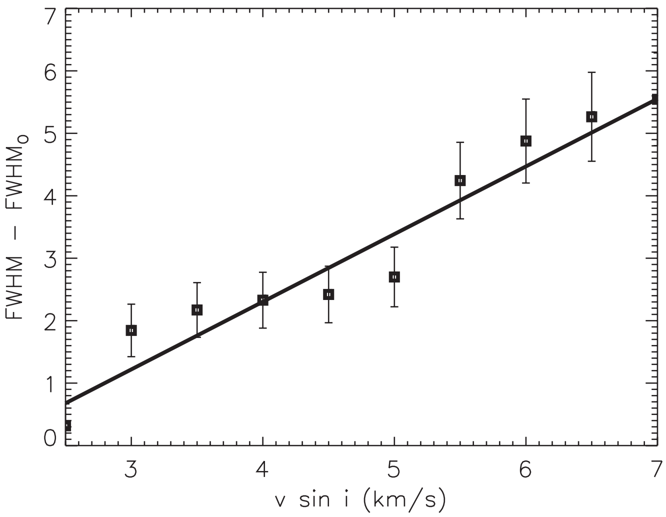


**Figure 5.** Change in the FWHM as a function of $v$ sin $i$. The squares show the average FWHM minus the initial FWHM ($FWHM_0$) after the profile has been broadened in steps of 0.5 km $s^{-1}$. The solid curve is the best straightline fit to the data.

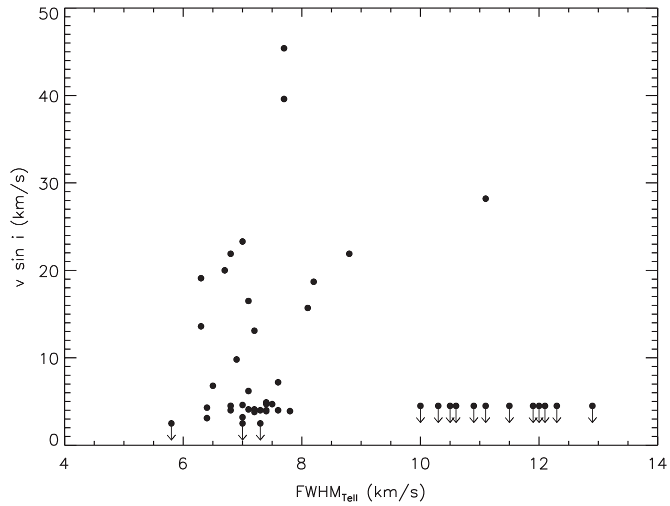


**Figure 6.** Distribution of $v$ sin $i$ as a function of the change in width of the instrumental profile. The width is parameterized by the FWHM of the telluric lines in km $s^{-1}$. No correlations are evident in the spread meaning the correction applied to the template spectrum appears robust. The symbols with downward pointing arrows indicate upper limits.

We decided not to use the arc lines for the IP measurements, since the calibrations are taken through a different optical path than the science images and therefore would not accurately model the intrinsic instrumental width (see Tull 1998 for HRS design). This procedure allowed us to determine that there was an increase in the instrumental width of almost a factor 2 between 2007 August 9 and 2007 October 17 due to poor thermal control in the HET spectrograph that lead to point-spread function instability through focus drift. The stars observed between these dates have a typical resolution limit of around 4–5 km $s^{-1}$; therefore, we employ a correction to each star to correct for the effects of the broadening of the IP.

Figure 5 shows the average change in the FWHM of a selection six stars with the highest S/N ratios as a function of $v$ sin $i$. Each of the data points mark the average of the FWHM difference ($FWHM-FWHM_0$) for the six stars, along with the associated scatter of the values, after broadening by rotation profiles in steps of 0.5 km $s^{-1}$, where $FWHM_0$ is the initial FWHM before any broadening has been applied. The solid line shows the best straightline fit to the data that we employed to correct for the IP, and is described by 1.08$x$–2.03, with an RMS scatter of only 0.46 km $s^{-1}$.

To employ these corrections, we determine the difference between the template telluric FWHM and that of each star. We then use this fit to determine by how much we must broaden the template profile to correct for the changing IP. Due to our resolution, this only becomes significant on the data mentioned above where the IP almost doubled in width, leaving such stars with a resolution of 4.5 km $s^{-1}$. These fits can also be used to determine the actual $v$ sin $i$ from the change in the FWHM compared to the template, at least in the low $v$ sin $i$ regime, and a test of this reveals agreement between both methods. The fits could be extended into the high $v$ sin $i$ regime in order to use this method to determine the rotational velocities for rapidly rotating stars also. All $v$ sin $i$s and their associated uncertainties are shown in Column 11 of Table 1, with the telluric FWHMs shown in Column 12 for reference.

Figure 6 shows the overall spread in the measured $v$ sin $i$ values as a function of the changing IP of the instrument. As mentioned above, the change in the IP is monitored by measuring the FWHM of the telluric lines in each spectrum ($FWHM_{Tell}$), and from the plot there appears no significant correlation between measured rotation values and the width of the IP. The linear correlation coefficient (r) for the entire sample is −0.12 and is still only 0.36 when removing all stars with measured upper limits, which are represented in the figure by the downward pointing arrows. This test highlights the lack of any significant correlation between the measured $v$ sin $i$s and the changing width of the IP. In fact, only one of the stars measured during the period of increased IP values is found to be above the detection threshold of our method, and as will be seen later; this correlates with the presence of H$\alpha$ in emission in this star.

None of these objects have previously determined $v$ sin $i$s with which to compare our values for an accuracy check. However, Rockenfeller et al. (2006) determined the $I$-band variability for the star LHS2930 and found the period to be 13 ± 2 hr. They also quote the radius of the star to be 0.33 $R_\odot$ from which we can estimate the rotation velocity assuming the variability is induced by the rotation of surface features such as star spots. Estimating this velocity in pure spherical geometry returns a value for the equatorial rotation velocity of $\sim 30^{+6}_{-3}$ km $s^{-1}$. We measure a velocity of 18.7 ± 1.5 km $s^{-1}$, which is significantly lower than the photometrically derived value. We note that the deconvolved line profile for this star is flagged as a low S/N. However, given these values, this would indicate the star is inclined to our line of sight by around $51^{+10}_{-7}{}^\circ$ ($i \sim 39^\circ$). Marcy & Butler (1996) show that for random stellar alignments, 68% of stars will have inclinations to our line of sight of below 47°, with 95% having inclinations above ∼20°, placing LHS2930 in between this 1 and 2$\sigma$ result and in agreement with the 1$\sigma$ value within the estimated uncertainty.

### *3.2. Hα Absorption/Emission*

In addition to selecting against stars with a large $v$ sin $i$, one might also like to monitor each star's magnetic activity through the absorption or emission in the H$\alpha$ line. The correlation between H$\alpha$ emission, age, activity, and rotational velocity has been well studied (e.g., Mohanty & Basri 2003; Reiners & Basri 2008 and refs therein); however, the magnetic field structure of M dwarfs, particularly slowly rotating M dwarfs, could be

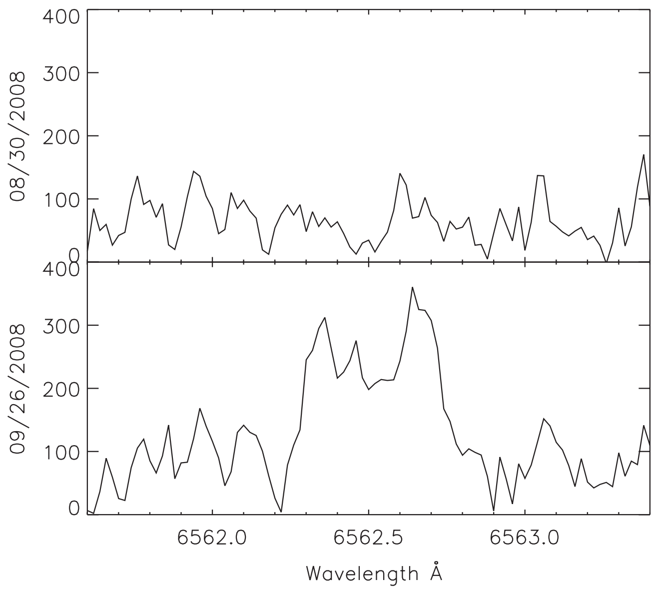


**Figure 7.** Region around the Hα-line profile for the star GJ1253 at two separate epochs. The top plot shows the first measurement made on 2008 August 30 and no Hα emission was found. However, the lower plot shows the second measurement made for this star one month later (2008 September 9) and clear emission is present.

complex, with magnetically active regions rotating in and out of view and the presence of strong flaring events. Also there is the possibility that a small percentage of our M dwarfs are being viewed close to pole-on, and instead of measuring their true $v \sin i$, which could be very high, we measure a smaller value and place these in the good planet search target bracket. Therefore, we searched for any emission, and also significant absorption, in the Hα line ($\lambda \sim 6562$ Å) in each of our target stars. Twenty four (43%) stars were found to show Hα emission, which includes the double profiles found for the active binary stars, and since such stars could be young and highly active, these may not be ideal stars to include in a precision radial-velocity planet search. Of these only six have rotation velocities below 10 km s$^{-1}$ (12% of the total). However, we do caution that we might be viewing active regions on these stars, or flaring outbursts, since numerous M stars across the spectral domain have been found to exhibit such phenomena (e.g., see Tinney et al. 1998; Martín & Ardila 2001; Osten et al. 2005). Further measurements may reveal these to vanish and therefore more epochs may be required to test if such stars have continuous Hα emission and are probably highly inclined young and active stars, or are simply going through a flaring event. Reiners (2009) has shown that flares only create significant noise at velocity precisions below 10 m s$^{-1}$ for moderate events and at the level of a few hundreds of m s$^{-1}$ for giant flares. However, giant flares are also heavily correlated with Hα variation and so can be easily removed from a radial-velocity campaign, albeit at the cost of precious observing time. Indeed, we may have viewed such a scenario in one of our stars GJ1253.

Figure 7 shows two epochs of spectroscopic measurements of the region around the Hα line for the star GJ1253. The upper panel is the first observation, made on 2008 August 30, whereas the lower panel shows the same region only one month later (2008 September 9). In the first observation there is no indication of any Hα emission present; however, only 27 days later when the second measurement was obtained, there is clear evidence for the Hα line in emission. Such a short period evolution of the line, coupled with the relatively low $v \sin i$ of the star

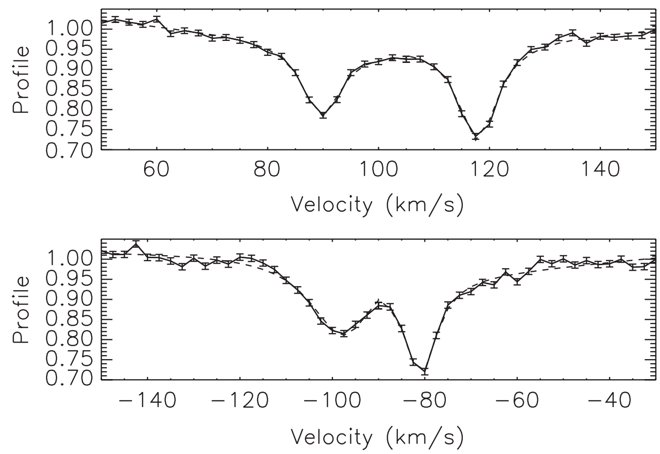


**Figure 8.** Example blended deconvolved profiles for two of the probable binary systems in this sample. The upper plot represents the star GJ1080 and has two clearly defined deep profiles, whereas the lower plot, which represents the LHS3080 system, has a secondary profile also, possibly from a weak signal contribution from the secondary. The dashed curves represent the best-fit double profiles to the data. The two other potential binaries have profiles with much larger separations.

($\leqslant 4.5$ km s$^{-1}$) may indicate that a small magnetic region is rotating in and out of view. If confirmed continuous monitoring of such Hα line changes could lead to the true rotation period of the star, removing the $\sin i$ degeneracy and giving both the true velocity and, for any discovered companions, their true masses without the need for continuous photometric monitoring. Note that Byrne et al. (1996) found variable Hα emission in the active M star HK Aquarii which they attribute to prominence-like clouds above the stellar surface that have characteristic timescales less than half the photometrically determined rotation period. It may be the case that such variability of Hα flux is mainly generated through flares or a changing magnetic field structure. Indeed, Hα variability for M stars is significant across the spectral domain, even on relatively short timescales (<60 minutes). Lee et al. (2009) find that ~80% of their mid-to-late M star sample exhibited statistically significant Hα variability. Therefore, if any correlation does exist between Hα variability and rotation velocity the characteristics must be sufficiently large such that typical short period small-scale variations do not mask it out.

Finally, we also searched for significant Hα absorption and found eight stars (14%) that show significant absorption. All of these have $v \sin i$s that would meet our criteria for planet search selection, as would be expected from a rotation–activity connection. Only, two out of the eight objects that exhibit significant Hα absorption are below our resolution limit, with a further three in agreement with the adopted resolution limit to within the estimated total uncertainty of the analysis technique. All stars with no Hα emission would meet our criteria for planet search selection, with the largest rotation rate of these coming from the M5 dwarf GJ1182 ($v \sin i = 6.8 \pm 0.5$ km s$^{-1}$). Column 13 of Table 1 shows the Hα emission flag, where either a detection was made or not, and stars with no significant emission which have asterisks show evidence for Hα absorption.

### *3.3. Spectroscopic Binaries*

There is the possibility that stars with multiple profiles are spectroscopic binaries of similar spectral type or stars with powerful magnetic fields. Figure 8 shows blended profiles found for both GJ1080 (upper panel) and LHS3080 (lower panel).

**Table 2**
M dwarf Binary Candidates

| Star | $V$ | $J$ | $H$ | $K_s$ | Spec Type | $\Delta v$ (km s$^{-1}$) | $v \sin i_{\rm pri}$ (km s$^{-1}$) | $v \sin i_{\rm sec}$ (km s$^{-1}$) | H$\alpha$ Emission |
|---|---|---|---|---|---|---|---|---|---|
| GJ1080 | 12.81 | 8.98 | 8.50 | 8.22 | M3.0 | 28.44 $\pm$ 0.28 | $\leqslant$3.0 | $\leqslant$3.0 | No |
| GJ3129 | 14.27 | 9.65 | 9.06 | 8.80 | M4.5 | 89.36 $\pm$ 0.78 | 5.2 $\pm$ 0.1 | 6.6 $\pm$ 0.3 | Yes - Double |
| Gl802 | 14.67 | 9.56 | 9.06 | 8.75 | M5.0 | 150.03 $\pm$ 1.19 | 6.4 $\pm$ 0.4 | $\leqslant$4.5 | Yes - Double |
| LHS3080 | 14.28 | 9.67 | 9.11 | 8.82 | M4.5 | 18.35 $\pm$ 0.32 | $\leqslant$3.0 | 3.8 $\pm$ 0.1 | Yes - Single |

It is clear that for both of these systems there is a primary deconvolved profile and a weaker secondary. To test if these are real rather than deconvolution artifacts, we split the spectra into two wavelength ranges, one spectrum covering the blue orders and one covering the red orders. By deconvolving both the red and blue spectra independently, we were able to confirm that these stars still exhibit double-lined profiles, lending weight to fact that the double profiles are due to real phenomena. The spectra for GJ1080 show double-lined profiles for atomic and molecular lines. The double-lined profiles for LHS3080 were difficult to confirm by eye in the spectrum. Along with both of these, there are another two binary systems, those of GJ3129 and Gl802. Both of these stars have double profiles, but with much wider separations, even though they exhibit noisier spectra. These are more clear cases than the previous two since they also have double H$\alpha$ emission profiles.

Gl802 was known to have a low-mass companion with an orbital period of $3.14 \pm 0.03$ yr (Pravdo et al. 2005), which was directly imaged by Lloyd et al. (2006). In addition, Ireland et al. (2008) have recently found this star to be part of a triple system, with a short period ($P \sim 19$ hr) spectroscopic companion. Our final deconvolution for this star is very noisy, in part due to the blended light from three different components with different spectral profiles. We do note however that there are two strong profiles in the final deconvolution (properties listed in Table 2) and potentially a further two weaker profiles. The weak profiles are only borderline significant due to the associated noise, but one might explain the short period binary found by Ireland et al. and the other, which is widely separated from the profile of Gl802A, could be an additional longer period companion.

McCarthy & Zuckerman (2004) surveyed both GJ3129 and LHS3080 as part of their AO campaign to detect substellar companions to a host of nearby young M dwarfs. They found no viable candidate to these stars between around 5″ and 15″ arcseconds. The lack of any viable detection around these, apparently young, stars is probably explained by the close separation of the objects, since the detectability of spectroscopic binaries is skewed toward short-period companions. Indeed, the LHS3080 profiles are blended with each other and since the secondary profile is significantly weaker than the primary, it is probably a much later and fainter companion object. The properties of these spectroscopic binaries are listed in Table 2, which include the Hipparcos $V$, Two Micron All Sky Survey (2MASS) $J$, $H$ and $K_s$ apparent magnitudes, their spectral types, the velocity separation of the double peaks along with their combined uncertainties, the $v \sin i$ estimates for both the primary star ($v \sin i_{\rm pri}$) and the secondary ($v \sin i_{\rm sec}$) and the H$\alpha$ flag. Note that the small uncertainties are an artifact of the blended fitting procedure and do not necessarily mean these values are more precise than the single profiles.

## 4. TEMPERATURE, MASS, AND METALLICITY

When performing radial-velocity searches for exoplanets other characteristics of the star determine radial-velocity limits e.g., the stellar mass. The mass of the primary determines the lower limit to the planetary mass for a given radial-velocity amplitude and therefore knowledge of the mass of any planet search target star is essential. We have determined the stellar mass for the bulk of our sample by utilizing relations between M star mass and their absolute magnitudes. To generate accurate absolute magnitudes, we searched the Yale Trigonometric Parallax project (van Altena et al. 1995), the RECONS list (Henry et al. 2006), and any parallaxes in the Gliese Catalogue of Nearby Stars to obtain accurate parallax measurements for all our candidates. The parallaxes, along with their associated uncertainties, are shown in Column 8 of Table 1, and these were used to determine the absolute magnitudes by converting them to distance and measuring the distance modulus. The photometry was acquired using both the Simbad[4] and VizieR[5] astronomical databases. The near-infrared photometry was taken from the 2MASS catalog (Skrutskie et al. 2006), and the $K_{\rm s}$ magnitudes were converted to $K$ using the calibrations in Carpenter (2001). The absolute $V$ and $K$ magnitudes were then input into the empirical mass relations from Delfosse et al. (2000), and two measurements of the mass for each star were determined. Both these measurements were averaged to get the final combined mass estimates for all objects with known parallax and their uncertainties were taken as the standard deviation of the two measurements. The uncertainties are typically $\pm$10%–15%, with a few of the closest stars having uncertainties down to the $\pm$1% level. Both the masses and their uncertainties are shown in Column 9 of Table 1.

Along with the mass, both the effective temperatures and metallicities ([Fe/H]) were estimated for the sample. The effective temperatures were determined using the $V{-}K_{\rm s}$ relation taken from Casagrande et al. (2008) and has a typical internal uncertainty of $\pm$17 K; however, the uncertainty on the overall accuracy of the technique will probably be substantially larger than this. The values with question marks next to them flag highly suspect effective temperatures. The [Fe/H] abundances were first determined photometrically using the color–magnitude relation in Bonfils et al. (2005). They quote the typical uncertainty for this method as $\pm$0.2 dex which we assign to all our metallicities shown in Column 10 of Table 1. Casagrande et al. also provide metallicities using their method, and these agree with the Bonfils et al. values within the quoted uncertainties. Note that recently Johnson & Apps (2009) claim that the Bonfils et al. relation may underestimate the metallicities of M dwarfs by as much as 0.3 dex. Finally, Table 1 also shows each star's $V$, $J$, $H$, and $K_s$ photometry.

## 5. RESULTS: $v \sin i$ DISTRIBUTIONS

Figure 9 shows the distribution of early-to-late M star rotation rates against their spectral type. The filled circles represent the stars in this work, and the open circles represent literature

4 Simbad Web site: http://simbad.u-strasbg.fr/simbad/.
5 VizieR Web site: http://webviz.u-strasbg.fr/viz-bin/VizieR.

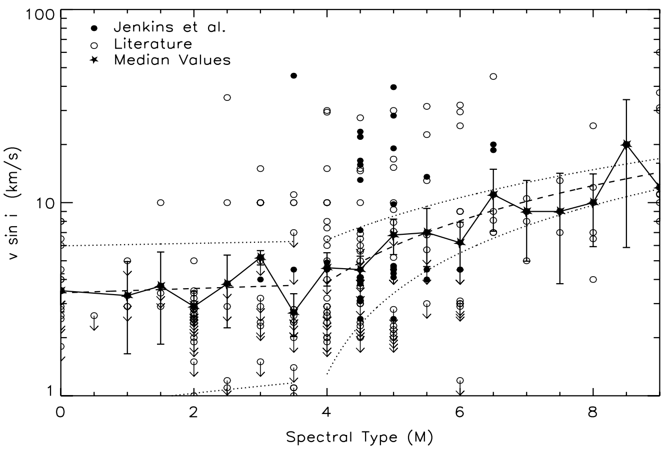


**Figure 9.** Distribution of $v \sin i$ against measured spectral type plotted in the log step. The values from this data are shown by the filled circles, with the literature values shown by the open circles. The trend of increasing rotation velocity with decreasing temperature is seen here and is highlighted by the solid line linking the filled stars. These stars mark the median values for all data in each spectral bin. The uncertainties plotted represent Poisson statistics, and the downward pointing arrows mark upper limits. Represented by the dashed lines are the best straightline fits to the medians for the early M dwarfs and mid-to-late M dwarfs, along with their standard $\pm 1\sigma$ uncertainties plotted by the dotted lines. The early Ms are found to have a much flatter distribution than the mid-to-late Ms, which are tending toward a more rising trend.

$v \sin i$s (from Stauffer & Hartmann 1986; Marcy & Chen 1992; Delfosse et al. 1998; Gizis et al. 2002; Mohanty & Basri 2003; Bailer-Jones 2004; Fuhrmeister & Schmitt 2004; Jones et al. 2005; Reiners 2007; West & Basri 2009). All literature $v \sin i$s are shown in Table 3 along with any measured $V$ magnitudes, 2MASS $J$, $H$, and $K_s$ photometry, spectral types, effective temperatures, parallaxes, masses, and [Fe/H] abundances, all determined using the same methods outlined above.

There is a large spread in $v \sin i$ across the mid-M star regime (M4.0–M6.5) compared with early M stars (<M4). The mid-M objects range from almost as high as over 50 km s$^{-1}$ and down as low as essentially zero km s$^{-1}$. The median dispersion of the $v \sin i$ distributions in the spectral-type bins between M0 and M3 is 3.70 ± 0.79 km s$^{-1}$, compared to the median dispersion of 9.00 ± 8.31 km s$^{-1}$ for bins at M4–M9.5. However, if we allow for a spectral typing uncertainty of ±0.5 sub-types and exclude both the M0 and M9.5 spectral bins, since they could be contaminated by K and L dwarfs, we find the dispersions are 3.70 ± 0.87 km s$^{-1}$ and 9.00 ± 4.37 km s$^{-1}$ respectively. A Kolmogorov–Smirnov (KS) test is run to compare these distributions and this returns a D-statistic of 0.539, giving an extremely low probability of only $1.396 \times 10^{-8}$% that the rotation rates for stars between M0.5 and M3 are drawn from the same parent population as those between M4 and M9. Also, a large fraction of stars with spectral types below M6.5, and particularly below the convective boundary region, only have measured upper limits. This will bias this result toward a noncorrelation, and so we can expect that with further detections at low velocities for these stars, this correlation will become more pronounced.

This step from low-to-high dispersions between M3 and M4 spectral types is thought to be due to the increased spindown timescale toward decreasing mass (Delfosse et al. 1998; Mohanty & Basri 2003) and that the spindown timescale is a significant fraction of the age of the young disk. Indeed, Donati et al. (2008) and Morin et al. (2008) have shown that the magnetic field topologies of early Ms (M0–M3) and mid-Ms (M4) are significantly different, with the early Ms having mainly toroidal and non-axisymmetric poloidal fields, whereas the M4s mainly exhibit axisymmetric poloidal fields. This result indicates a change in the magnetic field properties at the classical boundary between partially radiative and fully convective envelopes. If the spindown times are governed by the magnetic fields in this regime then a differing $v \sin i$ distribution might be expected. It might be the case that axisymmetric poloidal fields interact with the stellar wind more weakly than the toroidal, non-axisymmetric fields, driving a less efficient braking mechanism. Interestingly, a probe of the spindown timescale and the mechanism driving it can be made if we take the Delfosse et al. and Mohanty & Basri $v \sin i$ and $\log(L_{\mathrm{H}_\alpha}/L_{\mathrm{Bol}})$ values (Mohanty & Basri show the activities in these two works to be in excellent agreement). We can use these values to trace the rotational history for the fully convective, mid-M star regime (M4–M7). When the stars are binned into their respective spectral types, the trend found between these two quantities reveals a sharp saturation boundary (e.g., Figure 9 in Mohanty & Basri). By using Equation (3.1) in West et al. (2009), one can use the activity values to gain a statistical insight into the age distribution of these samples. In particular, the saturation boundary changes as a function of spectral type, increasing in velocity with increasing spectral type. Table 4 shows the spectral-type bins, along with the saturation boundary in velocity and activity lifetime ($l$) given in West et al. Due to the spindown of stars by the wind-braking mechanism, we can use this table to say that from a statistical footing, the average age of M4 stars with $v \sin i$s $\leqslant 8$ km s$^{-1}$ is older than 5 Gyr, M5s with velocities $\leqslant 10$ km s$^{-1}$, and M6s with velocities $\leqslant 12$ km s$^{-1}$, are older than 7 Gyr and M7s with velocities $\leqslant 13$ km s$^{-1}$ are older than 8 Gyr.

Figure 10 shows the $v \sin i$ values against spectral type for all stars in this study with a split made by their H$\alpha$ status. The filled circles represent all stars with no significant H$\alpha$ emission or absorption, the open circles represent stars with H$\alpha$ absorption, and the open stars represent objects with H$\alpha$ emission. The rotation–activity connection suggests a correlation between H$\alpha$ emission and the rotation velocity of cool M stars, and this is clearly seen in this plot. All stars with $v \sin i \geqslant 7$ km s$^{-1}$ are found to exhibit significant H$\alpha$ emission. Indeed, we have just shown that, on average, mid-to-late M stars with velocities $\geqslant 8$ km s$^{-1}$ are still in their young, active phase of evolution. No stars later than M5 were found to exhibit H$\alpha$ absorption, with five of these exhibiting no significant H$\alpha$ emission (55%). Such numbers correlate with previous results which suggest a high frequency of active M stars toward the latest spectral types (e.g., Fleming et al. 2000; Mohanty et al. 2002), even though we find a similar fraction of active M stars in all of our spectral bins. However, in our final M6.5 bin both stars are found to exhibit H$\alpha$ emission which agrees with the increasing trend of activity toward values approaching 100% at a spectral type of around M7. This increase in stars with H$\alpha$ in emission toward later spectral types appears to be a product of the fraction of young disk stars in this regime and also the increase in activity lifetime with increasing spectral type. From Table 4, we see that both the activity lifetime and the time spent in a state of high rotation increase with increasing spectral type. Such trends would naturally give rise to a larger fraction of stars with H$\alpha$ profiles in emission toward the latest M stars.

The filled stars in Figure 9 represent the median values in each spectral bin along with their associated Poisson errors.

**Table 3**
Table of $v$ sin $i$ Taken from the Literature and Used in This Work

| Star | $V$ | $J$ | $H$ | $K_s$ | Spec Type | $T_{EFF}$ (K) | $\pi$ (mas) | $M/M_\odot$ | [Fe/H] | $v$ sin $i$ (km $s^{-1}$) | Source |
|---|---|---|---|---|---|---|---|---|---|---|---|
| 2MASS−J1242081+290027 | ... | 16.42 | 16.03 | 15.45 | M8.0 | ... | ... | ... | ... | 7.0 | (f) |
| 2MASS−J1254012+250002 | ... | 15.29 | 14.80 | 14.81 | M7.5 | ... | ... | ... | ... | 13.0 | (f) |
| 2MASS−J1255583+275947 | ... | 15.42 | 14.73 | 14.58 | M7.5 | ... | ... | ... | ... | 9.0 | (f) |
| AD Leo | 9.43 | 5.45 | 4.84 | 4.59 | M4.5 | 3157 | 213.00 ± 4.00 | 0.390 ± 0.032 | 0.04 | 3.0 | (j) |
| BRI0021−0214 | 19.60 | 11.99 | 11.08 | 10.48 | M9.5 | 2092 | 80.00 ± 3.40 | 0.103 ± 0.031 | ... | 34.0 | (f) |
| BRI1222−1222 | ... | 12.57 | 11.82 | 11.35 | M9.0 | ... | ... | ... | ... | 8.0 | (f) |
| CTI0126+57.5 | ... | ... | ... | ... | M9.0 | ... | ... | ... | ... | 11.1 | (f) |
| CTI0156+28 | ... | 14.47 | 13.84 | 13.54 | M6.5 | ... | ... | ... | ... | 9.0 | (f) |
| CTI115638.4+28 | ... | 14.32 | 13.72 | 13.34 | M7.0 | ... | ... | ... | ... | 10.5 | (f) |
| CTI1539+28 | ... | 15.49 | 15.00 | 14.58 | M6.5 | ... | ... | ... | ... | 7.0 | (f) |
| CTI1747+28 | ... | 15.50 | 15.04 | 14.52 | M6.5 | ... | ... | ... | ... | 45.0 | (f) |
| CTI2332+27 | ... | 15.71 | 15.34 | 14.86 | M6.0 | ... | ... | ... | ... | 25.0 | (f) |
| DENIS-J0021−4243 | ... | 15.80 | 15.39 | 15.24 | M9.5 | ... | ... | ... | ... | 17.5 | (f) |
| DENIS−1048−3955 | ... | 14.60 | 14.23 | 14.19 | M8.0 | ... | ... | ... | ... | 25.0 | (h) |
| DENIS−J1207+0059 | ... | 10.38 | 10.13 | 10.06 | M9.0 | ... | ... | ... | ... | 10.0 | (f) |
| DENIS−J1431596−195321 | ... | 15.34 | 14.73 | 14.45 | M9.0 | ... | ... | ... | ... | 37.1 | (g) |
| ESO207−61 | 20.99 | 13.23 | 12.54 | 12.06 | M8.0 | ... | 70.00 ± 4.00 | 0.139 ± 0.088 | ... | 10.0 | (f) |
| G087−09B | ... | 10.40 | 9.79 | 9.76 | M4.0 | ... | ... | ... | ... | 6.0 | (i) |
| G089−032 | ... | 8.18 | 7.61 | 7.28 | M5.0 | ... | ... | ... | ... | 7.9 | (f) |
| G099−049 | ... | 6.91 | 6.31 | 6.04 | M4.0 | ... | ... | ... | ... | 7.4 | (f) |
| G165−08 | 12.19 | 7.56 | 7.00 | 6.72 | M4.0 | 2951 | 126.00 | 0.242 ± 0.018 | −0.02 | 55.5 | (f) |
| G188−38 | 11.98 | 7.64 | 7.04 | 6.78 | M4.0 | ... | ... | ... | ... | 29.4 | (f) |
| GJ65A | 12.57 | ... | ... | ... | M5.5 | ... | ... | ... | ... | 31.5 | (i) |
| GJ65B | 12.52 | ... | ... | ... | M6.0 | ... | ... | ... | ... | 29.5 | (i) |
| GJ166C | ... | 6.75 | 6.28 | 5.96 | M4.5 | ... | ... | ... | ... | 5.0 | (i) |
| GJ630.1A | ... | 8.50 | 8.04 | 7.80 | M4.5 | 2887* | ... | ... | ... | 27.5 | (i) |
| GJ699 | ... | 5.24 | 4.83 | 4.52 | M4.0 | ... | ... | ... | ... | ⩽ 2.8 | (f) |
| GJ725A | 8.91 | 5.19 | 4.74 | 4.41 | M3.0 | 3276 | 286.10 ± 1.80 | 0.342 ± 0.020 | −0.35 | ⩽ 5.0 | (i) |
| GJ725B | 9.69 | 5.72 | 5.20 | 4.98 | M3.5 | 3172 | 286.10 ± 1.80 | 0.266 ± 0.025 | −0.38 | ⩽ 7.0 | (i) |
| GJ896A | 10.35 | 6.16 | 5.57 | 5.31 | M3.5 | 3090 | 151.90 ± 3.70 | 0.378 ± 0.042 | 0.11 | 10.0 | (i) |
| GJ896B | ... | 7.10 | 6.56 | 6.26 | M4.5 | ... | ... | ... | ... | 15.0 | (i) |
| GJ1002 | 13.73 | 8.32 | 7.79 | 7.44 | M5.5 | ... | ... | ... | ... | ⩽ 3.0 | (f) |
| GJ1057 | 13.78 | 8.77 | 8.21 | 7.80 | M5.0 | 2706 | 120.00 ± 3.50 | 0.155 ± 0.005 | ... | ⩽ 2.2 | (f) |
| GJ1093 | 14.83 | 9.16 | 8.55 | 8.23 | M5.0 | ... | ... | ... | ... | ⩽ 2.8 | (f) |
| GJ1105 | 12.04 | 7.73 | 7.13 | 6.88 | M3.5 | ... | ... | ... | ... | ⩽ 2.0 | (c) |
| GJ1111 | 14.81 | 8.24 | 7.62 | 7.26 | M6.5 | ... | ... | ... | ... | 11.0 | (f) |
| GJ1111 | 14.81 | 8.24 | 7.62 | 7.26 | M6.5 | ... | ... | ... | ... | 8.1 | (c) |
| GJ1151 | 13.26 | 8.49 | 7.95 | 7.61 | M4.5 | 2767 | 120.00 ± 2.90 | 0.174 ± 0.001 | ... | ⩽ 4.1 | (f) |
| GJ1154A | 14.11 | 8.46 | 7.86 | 7.54 | M5.0 | ... | ... | ... | ... | 5.2 | (f) |
| GJ1156 | 13.79 | 8.52 | 7.88 | 7.54 | M5.0 | 2632 | 150.00 ± 3.00 | 0.139 ± 0.006 | ... | 9.2 | (f) |
| GJ1224 | 13.64 | 8.64 | 8.09 | 7.81 | M4.5 | 2711 | 130.00 ± 3.70 | 0.148 ± 0.004 | ... | ⩽ 5.6 | (f) |
| GJ1227 | 13.40 | 8.64 | 8.05 | 7.71 | M4.5 | 2910 | 120.00 ± 2.20 | 0.167 ± 0.002 | ... | ⩽ 2.3 | (f) |
| GJ1230B | 14.40 | 8.86 | 8.03 | 7.73 | M5.0 | 2714 | 120.00 ± 7.20 | 0.147 ± 0.024 | ... | ⩽ 7.1 | (f) |
| GJ1245A | 13.41 | 7.79 | 7.19 | 6.82 | M5.5 | 2695 | 220.00 ± 1.00 | 0.129 ± 0.010 | ... | 22.5 | (f) |
| GJ1245B | 13.99 | 8.27 | 7.73 | 7.36 | M5.5 | 2673 | 220.00 ± 1.00 | 0.108 ± 0.001 | ... | 6.8 | (f) |
| GJ1286 | 14.68 | 9.15 | 8.51 | 8.15 | M5.5 | 2716 | 140.00 ± 3.50 | 0.116 ± 0.001 | ... | ⩽ 5.7 | (f) |
| GJ1289 | 12.67 | 8.11 | 7.45 | 7.20 | M4.0 | 2969 | 120.00 ± 2.90 | 0.209 ± 0.004 | ... | ⩽ 2.6 | (f) |
| GJ2005 | ... | 9.25 | 8.55 | 8.24 | M6.0 | ... | ... | ... | ... | 9.0 | (f) |
| GJ2066 | 10.05 | 6.63 | 6.04 | 5.74 | M2.0 | 3420 | 114.00 ± 3.90 | 0.447 ± 0.005 | −0.22 | ⩽ 2.7 | (c) |
| GJ2069B | 13.40 | 8.62 | 8.05 | 7.72 | M4.0 | 2904 | ... | ... | ... | 6.5 | (f) |
| GJ2097 | 12.54 | ... | ... | ... | M1.5 | ... | ... | ... | ... | ⩽ 3.7 | (c) |
| GJ3136 | 12.47 | 8.42 | 7.81 | 7.55 | M5.0 | 3141 | 70.00 ± 4.00 | 0.312 ± 0.006 | −0.14 | 30.0 | (e) |
| GJ3304 | 12.51 | 8.17 | 7.62 | 7.30 | M4.0 | 3038 | 100.00 ± 7.00 | 0.243 ± 0.002 | −0.14 | 30.0 | (e) |
| GJ3323 | 12.16 | 7.62 | 7.07 | 6.71 | M4.0 | 2975 | 163.00 ± 6.00 | 0.196 ± 0.002 | ... | ⩽ 3.2 | (f) |
| GJ3378 | 11.71 | 7.47 | 6.95 | 6.62 | M3.5 | 3072 | 132.20 ± 2.90 | 0.255 ± 0.002 | −0.18 | ⩽ 2.7 | (c) |
| GJ3482B | 11.20 | 7.34 | 6.76 | 6.50 | M2.5 | 3216 | 59.00 ± 7.00 | 0.532 ± 0.066 | ... | 35.0 | (e) |
| GJ3622 | 15.60 | 8.86 | 8.26 | 7.90 | M6.0 | ... | 220.00 ± 3.60 | ... | ... | 3.0 | (f) |
| GJ3828B | ... | 13.09 | 12.53 | 12.09 | M6.0 | ... | ... | ... | ... | 9.0 | (f) |
| GJ3877 | 17.05 | 9.97 | 9.31 | 8.93 | M7.0 | 2393 | ... | ... | ... | 8.0 | (f) |
| GJ4281 | 17.14 | 10.77 | 10.22 | 9.81 | M6.5 | 2536 | 90.00 ± 4.90 | 0.093 ± 0.005 | ... | 7.0 | (f) |
| Gl14 | 8.94 | 6.39 | 5.75 | 5.56 | M0.5 | 4021 | 70.00 ± 3.90 | 0.721 ± 0.029 | −0.30 | ⩽ 2.6 | (b) |
| Gl15A | 8.07 | 5.25 | 4.48 | 4.02 | M2.0 | ... | ... | ... | ... | 2.9 | (c) |
| Gl15B | 11.04 | 6.79 | 6.19 | 5.95 | M6.0 | ... | ... | ... | ... | ⩽ 3.1 | (c) |
| Gl26 | 11.06 | 7.45 | 6.86 | 6.61 | M4.0 | ... | ... | ... | ... | ⩽ 2.9 | (b) |
| Gl48 | 9.96 | 6.30 | 5.70 | 5.42 | M3.0 | 3303 | 115.50 ± 3.70 | 0.480 ± 0.030 | 0.04 | ⩽ 2.4 | (c) |

**Table 3**
(Continued)

| Star | $V$ | $J$ | $H$ | $K_s$ | Spec Type | $T_{EFF}$ (K) | $\pi$ (mas) | $M/M_\odot$ | [Fe/H] | $v \sin i$ (km s$^{-1}$) | Source |
|---|---|---|---|---|---|---|---|---|---|---|---|
| Gl49 | 9.56 | 6.23 | 5.58 | 5.37 | M1.5 | 3468 | ... | ... | ... | $\leqslant$ 3.4 | (c) |
| Gl70 | 10.96 | 7.37 | 6.81 | 6.49 | M2.0 | 3335 | 90.00 ± 5.10 | 0.403 ± 0.003 | −0.22 | $\leqslant$ 3.0 | (c) |
| Gl82 | 12.04 | 7.79 | 7.22 | 6.94 | M4.0 | 3069 | 78.50 ± 4.90 | 0.349 ± 0.035 | 0.06 | 15.0 | (a) |
| Gl83.1 | 12.26 | 7.51 | 6.97 | 6.65 | M4.5 | ... | ... | ... | ... | 3.8 | (f) |
| Gl87 | 10.03 | 6.83 | 6.32 | 6.06 | M2.5 | 3542 | 86.70 ± 7.40 | 0.512 ± 0.022 | −0.35 | $\leqslant$ 1.1 | (b) |
| Gl105B | 11.66 | 7.33 | 6.79 | 6.55 | M4.5 | 3042 | 129.40 ± 4.30 | 0.266 ± 0.003 | −0.14 | $\leqslant$ 2.4 | (f) |
| Gl109 | 10.58 | 6.75 | 6.20 | 5.94 | M3.5 | 3228 | 130.00 ± 4.20 | 0.359 ± 0.002 | −0.21 | $\leqslant$ 2.8 | (c) |
| Gl157B | 11.48 | 7.77 | 7.16 | 6.90 | M3.0 | 3280 | 70.00 ± 5.20 | 0.416 ± 0.012 | −0.10 | $\leqslant$ 10.0 | (a) |
| Gl169.1A | 11.08 | 6.62 | 6.01 | 5.69 | M4.0 | 3000 | 180.00 ± 0.80 | 0.271 ± 0.025 | 0.01 | 1.9 | (f) |
| Gl205 | 7.92 | 5.00 | 4.15 | 4.04 | M1.5 | ... | ... | ... | ... | 1.0 | (j) |
| Gl206 | 11.48 | 7.42 | 6.88 | 6.53 | M4.0 | 3137 | 70.00 ± 3.90 | 0.452 ± 0.063 | 0.27 | 10.0 | (a) |
| Gl207.1 | 11.52 | 7.76 | 7.15 | 6.83 | M2.5 | 3258 | 60.00 ± 5.20 | 0.473 ± 0.044 | 0.15 | 10.0 | (a) |
| Gl213 | 11.48 | 7.12 | 6.63 | 6.39 | M4.0 | ... | ... | ... | ... | $\leqslant$ 2.9 | (f) |
| Gl229A | 8.14 | 5.10 | 4.39 | 4.17 | M1/M2 | 3571 | 173.19 ± 1.12 | 0.583 ± 0.005 | −0.09 | 1.0 | (j) |
| Gl232 | 13.06 | 8.66 | 8.16 | 7.89 | M4.5 | 3019 | 120.00 ± 2.30 | 0.168 ± 0.023 | ... | $\leqslant$ 3.1 | (f) |
| Gl234A | 11.10 | 6.38 | 5.75 | 5.46 | M4.5 | 2923 | 240.00 ± 3.70 | 0.224 ± 0.020 | 0.00 | 6.0 | (f) |
| Gl251 | 9.89 | 6.10 | 5.53 | 5.26 | M4.0 | 3245 | 170.00 ± 3.20 | 0.372 ± 0.002 | −0.18 | $\leqslant$ 2.4 | (c) |
| Gl268.3 | 10.83 | 7.01 | 6.44 | 6.17 | M0.0 | 3232 | 126.00 ± 5.00 | 0.337 ± 0.007 | −0.25 | $\leqslant$ 2.5 | (d) |
| Gl273 | 9.89 | 5.71 | 5.22 | 4.83 | M3.5 | 3093 | 264.40 ± 2.00 | 0.286 ± 0.007 | −0.12 | 0.0 | (j) |
| Gl277A | 11.87 | 6.77 | 6.18 | 5.90 | M3.5 | 2819 | 90.00 ± 2.50 | 0.413 ± 0.142 | ... | $\leqslant$ 10.0 | (a) |
| Gl277B | 11.79 | 7.57 | 6.99 | 6.74 | M4.5 | 3079 | 90.00 ± 2.50 | 0.338 ± 0.026 | 0.00 | $\leqslant$ 10.0 | (a) |
| Gl285 | 11.12 | 6.58 | 6.01 | 5.67 | M4.5 | 2975 | 170.00 ± 4.40 | 0.284 ± 0.035 | 0.07 | 6.5 | (f) |
| Gl299A | 12.83 | 8.42 | 7.93 | 7.64 | M4.5 | 3036 | 148.00 ± 2.60 | 0.155 ± 0.025 | ... | 3.0 | (f) |
| Gl338A | 7.64 | 4.89 | 3.99 | 3.96 | M0.0 | 3851 | 162.50 ± 2.00 | 0.660 ± 0.011 | −0.17 | 2.9 | (c) |
| Gl338B | 7.74 | 4.78 | 4.04 | 4.13 | M0.0 | 3695 | 162.50 ± 2.00 | 0.634 ± 0.028 | −0.35 | 2.8 | (c) |
| Gl362 | 11.36 | 7.33 | 6.73 | 6.44 | M3.0 | 3148 | 80.00 ± 3.50 | 0.423 ± 0.048 | 0.16 | $\leqslant$ 10.0 | (a) |
| Gl369 | 10.00 | 6.99 | 6.40 | 6.12 | M2.0 | 3661 | 84.80 ± 7.60 | 0.517 ± 0.031 | −0.42 | 5.0 | (b) |
| Gl382 | 9.26 | 5.89 | 5.26 | 4.98 | M2.0 | 3446 | 120.00 ± 5.90 | 0.556 ± 0.027 | 0.07 | 1.3 | (j) |
| Gl393 | 9.63 | 6.18 | 5.61 | 5.28 | M2.5 | 3404 | 130.00 ± 5.10 | 0.473 ± 0.008 | −0.12 | $\leqslant$ 1.1 | (j) |
| Gl402 | 11.66 | 7.32 | 6.71 | 6.34 | M5.0 | 3038 | 145.10 ± 4.80 | 0.255 ± 0.014 | −0.06 | $\leqslant$ 2.3 | (f) |
| Gl406 | 13.54 | 7.09 | 6.48 | 6.04 | M6.0 | 2520 | 418.30 ± 2.50 | 0.101 ± 0.005 | ... | $\leqslant$ 3.0 | (f) |
| Gl406 | 13.54 | 7.09 | 6.48 | 6.08 | M6.0 | 2520 | 418.30 ± 2.50 | 0.101 ± 0.005 | ... | $\leqslant$ 2.9 | (c) |
| Gl408 | 10.03 | 6.31 | 5.76 | 5.47 | M3.0 | 3276 | 140.00 ± 4.30 | 0.406 ± 0.007 | −0.14 | $\leqslant$ 2.3 | (c) |
| Gl411 | 7.49 | 4.20 | 3.64 | 3.22 | M2.0 | 3490 | 397.30 ± 1.80 | 0.421 ± 0.017 | −0.33 | $\leqslant$ 2.9 | (c) |
| Gl412A | 8.68 | 5.54 | 5.00 | 4.77 | M2.0 | ... | ... | ... | ... | $\leqslant$ 3.0 | (c) |
| Gl412B | 14.45 | 8.74 | 8.18 | 7.84 | M6.0 | ... | ... | ... | ... | 7.7 | (f) |
| Gl414B | 9.95 | 6.59 | 5.97 | 5.70 | M2.0 | 3451 | 70.00 ± 3.60 | 0.636 ± 0.050 | ... | $\leqslant$ 3.2 | (b) |
| Gl424 | 9.32 | 6.31 | 5.73 | 5.53 | M1.0 | ... | ... | ... | ... | $\leqslant$ 2.9 | (c) |
| Gl436 | 10.68 | 6.90 | 6.32 | 6.07 | M3.5 | ... | ... | ... | ... | $\leqslant$ 1.0 | (b) |
| Gl445 | 10.78 | 6.72 | 6.22 | 5.93 | M4.0 | 3137 | 190.00 ± 6.00 | 0.254 ± 0.018 | −0.31 | $\leqslant$ 2.0 | (c) |
| Gl447 | 11.08 | 6.51 | 5.95 | 5.62 | M4.5 | 2966 | 300.00 ± 1.70 | 0.179 ± 0.007 | ... | $\leqslant$ 2.0 | (f) |
| Gl450 | 9.78 | 6.42 | 5.83 | 5.59 | M1.0 | 3451 | 110.00 ± 5.70 | 0.491 ± 0.004 | −0.21 | $\leqslant$ 3.3 | (c) |
| Gl459.3 | 10.62 | 7.67 | 6.97 | 6.77 | M2.0 | 3702 | 50.00 ± 1.60 | 0.604 ± 0.008 | −0.18 | $\leqslant$ 2.8 | (b) |
| Gl461AB | 9.19 | 6.86 | 6.22 | 6.01 | M0.0 | ... | ... | ... | ... | $\leqslant$ 2.5 | (b) |
| Gl464 | 10.43 | 7.48 | 6.86 | 6.60 | M2.0 | 3702 | 49.30 ± 4.10 | 0.641 ± 0.001 | −0.08 | $\leqslant$ 2.4 | (b) |
| Gl480 | 11.52 | 7.58 | 6.94 | 6.66 | M4.0 | 3183 | 80.00 ± 6.10 | 0.394 ± 0.031 | 0.04 | $\leqslant$ 0.8 | (b) |
| Gl486 | 11.40 | 7.20 | 6.67 | 6.33 | M4.0 | 3086 | 120.00 ± 4.00 | 0.311 ± 0.017 | −0.06 | $\leqslant$ 2.0 | (c) |
| Gl487 | 10.92 | 6.88 | 6.23 | 6.05 | M3.0 | 3145 | 116.20 ± 0.50 | 0.365 ± 0.021 | −0.04 | 10.0 | (a) |
| Gl490A | 10.50 | 7.40 | 6.73 | 6.52 | M0.0 | 3603 | 50.00 ± 3.60 | 0.639 ± 0.018 | 0.07 | 8.0 | (a) |
| Gl490B | 13.16 | 8.87 | 8.28 | 7.99 | M4.0 | 3055 | 50.00 ± 3.60 | 0.336 ± 0.036 | 0.07 | 10.0 | (a) |
| Gl493.1 | 13.37 | 8.55 | 7.97 | 7.63 | M5.0 | 2893 | 120.00 ± 3.50 | 0.170 ± 0.002 | ... | 16.8 | (f) |
| Gl494 | 9.72 | 6.44 | 5.79 | 5.55 | M1.5 | 3496 | 90.00 ± 5.80 | 0.572 ± 0.020 | 0.03 | 10.0 | (a) |
| Gl507.1 | 10.66 | 7.27 | 6.64 | 6.36 | M2.0 | 3435 | 50.00 ± 7.50 | 0.645 ± 0.058 | ... | $\leqslant$ 2.6 | (b) |
| Gl514 | 9.04 | 5.90 | 5.30 | 5.01 | M1.0 | 3578 | 138.70 ± 2.90 | 0.514 ± 0.014 | −0.28 | 1.3 | (j) |
| Gl521 | 10.26 | 7.05 | 6.51 | 6.26 | M2.0 | 3536 | 80.00 ± 5.30 | 0.506 ± 0.021 | −0.34 | $\leqslant$ 2.0 | (b) |
| Gl526 | 8.46 | 5.18 | 4.78 | 4.42 | M4.0 | ... | ... | ... | ... | 1.4 | (j) |
| Gl552 | 10.68 | 7.23 | 6.61 | 6.36 | M2.5 | 3404 | 70.00 ± 4.40 | 0.517 ± 0.019 | −0.01 | $\leqslant$ 1.2 | (b) |
| Gl555 | 11.35 | 6.84 | 6.26 | 5.91 | M4.0 | 2984 | 160.00 ± 7.90 | 0.273 ± 0.029 | 0.03 | 2.7 | (f) |
| Gl569AB | 10.20 | 6.63 | 5.99 | 5.74 | M2.5 | 3345 | 95.60 ± 1.40 | 0.499 ± 0.028 | 0.05 | $\leqslant$ 3.8 | (b) |
| Gl570.2 | 11.08 | 8.44 | 7.82 | 7.64 | M2.0 | 3942 | 70.00 ± 5.00 | 0.378 ± 0.108 | −1.21 | $\leqslant$ 2.5 | (b) |
| Gl570B | 8.10 | 4.55 | 3.91 | 3.80 | M2.0 | ... | ... | ... | ... | $\leqslant$ 2.9 | (b) |
| Gl581 | 10.56 | 6.71 | 6.09 | 5.81 | M5.0 | 3220 | 160.00 ± 5.60 | 0.313 ± 0.007 | −0.24 | $\leqslant$ 2.1 | (c) |
| Gl623 | 10.27 | 6.64 | 6.14 | 5.92 | M3.0 | ... | ... | ... | ... | $\leqslant$ 2.9 | (c) |
| Gl625 | 10.17 | 6.61 | 6.06 | 5.81 | M2.0 | 3350 | 150.00 ± 2.50 | 0.349 ± 0.030 | −0.44 | $\leqslant$ 3.4 | (c) |
| Gl628 | 10.12 | 5.95 | 5.37 | 5.04 | M3.5 | 3097 | 240.00 ± 4.20 | 0.286 ± 0.009 | −0.11 | 1.1 | (j) |

**Table 3**
(Continued)

| Star | $V$ | $J$ | $H$ | $K_s$ | Spec Type | $T_{EFF}$ (K) | $\pi$ (mas) | $M/M_\odot$ | [Fe/H] | $v \sin i$ (km s$^{-1}$) | Source |
|---|---|---|---|---|---|---|---|---|---|---|---|
| Gl643 | 11.70 | 7.55 | 7.06 | 6.70 | M4.0 | 3104 | 171.90 ± 7.30 | 0.201 ± 0.023 | ... | ≤ 2.7 | (c) |
| Gl649 | 9.62 | 6.45 | 5.86 | 5.60 | M2.0 | 3560 | 100.00 ± 4.30 | 0.534 ± 0.009 | −0.23 | ≤ 1.9 | (b) |
| Gl654 | 10.07 | 6.78 | 6.19 | 5.95 | M3.5 | 3490 | 100.00 ± 7.80 | 0.471 ± 0.018 | −0.33 | ≤ 1.1 | (b) |
| Gl669A | 11.42 | 7.27 | 6.71 | 6.39 | M4.0 | 3104 | 93.30 ± 1.90 | 0.376 ± 0.040 | 0.09 | ≤ 10.0 | (a) |
| Gl669B | 13.02 | 7.27 | 6.71 | 6.39 | M5.0 | 2667 | 93.30 ± 1.90 | 0.311 ± 0.132 | ... | ≤ 10.0 | (a) |
| Gl686 | 9.62 | 6.36 | 5.79 | 5.55 | M1.0 | 3507 | 130.00 ± 3.80 | 0.447 ± 0.030 | −0.44 | ≤ 5.0 | (c) |
| Gl687 | 9.15 | 5.34 | 4.77 | 4.53 | M3.5 | 3237 | 212.70 ± 2.00 | 0.407 ± 0.013 | −0.09 | ≤ 2.8 | (c) |
| Gl694 | 10.50 | 6.81 | 6.22 | 5.93 | M3.5 | 3289 | 100.00 ± 4.10 | 0.447 ± 0.022 | −0.02 | ≤ 1.4 | (b) |
| Gl701 | 9.37 | 6.16 | 5.57 | 5.28 | M2.0 | 3536 | 130.00 ± 4.30 | 0.489 ± 0.016 | −0.30 | ≤ 3.5 | (c) |
| Gl720A | 9.84 | 6.88 | 6.26 | 6.06 | M2.0 | 3695 | 67.80 ± 2.10 | 0.617 ± 0.012 | −0.21 | ≤ 1.5 | (b) |
| Gl735 | 10.20 | 6.31 | 5.68 | 5.40 | M3.0 | 3203 | 90.00 ± 2.70 | 0.557 ± 0.087 | ... | ≤ 10.0 | (a) |
| Gl745A | 10.84 | 7.30 | 6.73 | 6.50 | M2.0 | 3359 | 110.00 ± 4.10 | 0.348 ± 0.032 | −0.46 | ≤ 3.0 | (c) |
| Gl745B | 10.77 | 7.28 | 6.75 | 6.50 | M2.0 | 3384 | 110.00 ± 4.10 | 0.352 ± 0.037 | −0.50 | 2.8 | (c) |
| Gl748 | 11.06 | 7.09 | 6.57 | 6.27 | M4.0 | 3172 | 100.00 ± 2.40 | 0.384 ± 0.021 | −0.04 | 4.6 | (b) |
| Gl752A | 9.13 | 5.58 | 4.93 | 4.64 | M3.5 | 3354 | 176.70 ± 2.40 | 0.460 ± 0.018 | −0.04 | ≤ 2.6 | (c) |
| Gl781 | 11.97 | 8.83 | 8.35 | 8.09 | M3.0 | 3578 | 59.90 ± 2.00 | 0.338 ± 0.074 | −0.87 | 15.0 | (a) |
| Gl791.2 | 13.04 | 8.23 | 7.67 | 7.28 | M6.0 | 2896 | 110.00 ± 1.90 | 0.210 ± 0.020 | 0.01 | 32.0 | (f) |
| Gl793 | 10.44 | 6.74 | 6.14 | 5.91 | M3.0 | 3284 | 120.00 ± 3.10 | 0.393 ± 0.001 | −0.20 | ≤ 3.2 | (c) |
| Gl806 | 10.84 | 7.33 | 6.77 | 6.51 | M3.0 | 3374 | 80.00 ± 2.20 | 0.446 ± 0.004 | −0.21 | ≤ 1.5 | (b) |
| Gl809 | 8.54 | 5.43 | 4.92 | 4.60 | M2.0 | 3597 | 130.00 ± 3.60 | 0.614 ± 0.006 | −0.06 | ≤ 2.8 | (c) |
| Gl812A | 11.87 | 7.82 | 7.31 | 7.04 | M3.0 | 3141 | 60.00 ± 5.10 | 0.431 ± 0.042 | 0.12 | ≤ 10.0 | (a) |
| Gl815A | 10.10 | 6.67 | 6.09 | 5.86 | M3.0 | 3414 | 70.00 ± 3.30 | 0.608 ± 0.039 | ... | ≤ 10.0 | (a) |
| Gl829 | 10.35 | 6.25 | 5.74 | 5.43 | M4.0 | 3122 | 150.00 ± 4.80 | 0.371 ± 0.028 | 0.01 | ≤ 4.0 | (c) |
| Gl849 | 10.42 | 6.51 | 5.90 | 5.56 | M3.5 | 3195 | 120.00 ± 3.30 | 0.426 ± 0.044 | 0.13 | ≤ 2.4 | (c) |
| Gl851 | 10.29 | 6.72 | 6.03 | 5.79 | M2.0 | 3345 | 80.00 ± 2.60 | 0.554 ± 0.053 | ... | ≤ 2.5 | (b) |
| Gl860A | 9.59 | 5.57 | 5.04 | 4.76 | M2.0 | 3152 | 10.00 ± 4.50 | ... | ... | ≤ 3.0 | (c) |
| Gl860B | 10.30 | 5.57 | 5.04 | 4.76 | M4.0 | 2919 | 10.00 ± 4.50 | ... | ... | 4.7 | (f) |
| Gl863 | 10.36 | 7.21 | 6.60 | 6.33 | M0.0 | 3572 | 70.00 ± 3.70 | 0.541 ± 0.006 | −0.20 | ≤ 1.8 | (b) |
| Gl873 | 10.09 | 6.11 | 5.55 | 5.28 | M4.5 | 3168 | 200.00 ± 2.60 | 0.315 ± 0.002 | −0.20 | 6.9 | (c) |
| Gl875.1 | 11.78 | 7.70 | 7.13 | 6.85 | M3.5 | 3130 | 70.00 ± 3.00 | 0.405 ± 0.042 | 0.11 | 11.0 | (a) |
| Gl876 | 10.17 | 5.93 | 5.35 | 4.98 | M5.0 | 3172 | 210.00 ± 5.40 | 0.322 ± 0.032 | 0.04 | ≤ 2.0 | (f) |
| Gl880 | 8.66 | 5.36 | 4.80 | 4.52 | M2.0 | ... | ... | ... | ... | ≤ 2.8 | (c) |
| Gl905 | 12.28 | 6.88 | 6.25 | 5.90 | M6.0 | 2746 | 320.00 ± 1.10 | 0.136 ± 0.008 | ... | ≤ 1.2 | (c) |
| Gl908 | 8.98 | 5.83 | 5.28 | 5.02 | M2.0 | 3572 | 177.90 ± 5.60 | 0.431 ± 0.046 | −0.58 | ≤ 3.0 | (c) |
| LHS1885 | 13.65 | 8.59 | 7.99 | 7.66 | M4.5 | 2733* | 90.00 ± 2.30 | 0.208 ± 0.031 | 0.07 | ≤ 3.7 | (f) |
| LHS2065 | ... | 11.21 | 10.47 | 9.94 | M9.0 | ... | ... | ... | ... | 12.0 | (f) |
| LHS2243 | ... | 11.99 | 11.33 | 10.95 | M7.5 | 1846** | ... | ... | ... | 7.0 | (f) |
| LHS2397A | 19.57 | 11.93 | 11.23 | 10.68 | M8.5 | ... | 70.00 ± 2.10 | ... | ... | 20.0 | (f) |
| LHS2520 | 12.06 | 7.77 | 7.14 | 6.86 | M3.5 | 3033 | ... | ... | ... | ≤ 2.0 | (c) |
| LHS2632 | ... | 12.23 | 11.58 | 11.21 | M7.0 | 1969** | ... | ... | ... | 5.0 | (f) |
| LHS2645 | 18.80 | 12.19 | 11.55 | 11.16 | M7.0 | 2487 | ... | ... | ... | 9.0 | (f) |
| LHS2924 | 19.58 | 11.99 | 11.23 | 10.69 | M9.0 | 1665** | 90.00 ± 1.30 | 0.105 ± 0.043 | ... | 11.0 | (f) |
| LHS3376 | 13.46 | 8.74 | 8.26 | 7.93 | M4.5 | 2922 | 140.00 ± 5.30 | 0.139 ± 0.017 | ... | 14.6 | (f) |
| LP229−17 | 11.75 | 7.18 | 6.53 | 7.10 | M3.5 | 3265 | 138.00 ± 40.00 | 0.214 ± 0.046 | −0.54 | ≤ 2.0 | (c) |
| LP412−31 | 19.21 | 11.76 | 11.07 | 10.64 | M8.0 | 2191* | ... | ... | ... | 12.0 | (f) |
| LP467−16 | 13.59 | 9.08 | 8.51 | 8.21 | M5.0 | 2984 | ... | ... | ... | 15.2 | (f) |
| LP731−47 | ... | ... | ... | ... | M6.5 | ... | ... | ... | ... | 11.0 | (f) |
| LP759−25 | ... | 11.66 | 11.05 | 10.72 | M5.5 | ... | ... | ... | ... | 13.0 | (f) |
| LP944−20 | ... | 10.73 | 10.02 | 9.55 | M9.0 | 1764* | ... | ... | ... | 31.0 | (f) |
| RG0050−2722 | ... | 13.61 | 12.98 | 12.54 | M8.0 | ... | ... | ... | ... | 4.0 | (f) |
| SDSS011012.22−085627.5 | ... | 14.78 | 14.22 | 13.86 | M7.0 | ... | ... | ... | ... | ≤ 3.5 | (k) |
| SDSS021749.99−084409.4 | 19.04 | 14.20 | 13.63 | 13.30 | M6.0 | ... | ... | ... | ... | 4.0 ± 0.5 | (k) |
| SDSS023908.41−072429.3 | ... | 14.81 | 14.21 | 13.76 | M7.0 | ... | ... | ... | ... | ≤ 3.5 | (k) |
| SDSS072543.94+382511.4 | ... | 12.72 | 12.12 | 11.83 | M7.0 | ... | ... | ... | ... | ≤ 3.5 | (k) |
| SDSS083231.52+474807.7 | 17.56 | 12.41 | 11.79 | 11.45 | M6.0 | ... | ... | ... | ... | 4.0 ± 0.5 | (k) |
| SDSS094720.07−002009.5 | ... | 12.26 | 11.63 | 11.35 | M7.0 | ... | ... | ... | ... | 6.5 ± 0.5 | (k) |
| SDSS094738.45+371016.5 | ... | 12.19 | 11.67 | 11.34 | M7.0 | ... | ... | ... | ... | 6.0 ± 0.5 | (k) |
| SDSS110153.86+341017.1 | ... | 12.78 | 12.20 | 11.99 | M7.0 | ... | ... | ... | ... | ≤ 3.5 | (k) |
| SDSS112036.08+072012.7 | ... | ... | ... | ... | M7.0 | ... | ... | ... | ... | ≤ 3.5 | (k) |
| SDSS125855.13+052034.7 | ... | 12.64 | 12.06 | 11.69 | M7.0 | ... | ... | ... | ... | ≤ 3.5 | (k) |
| SDSS151727.72+335702.4 | ... | 12.76 | 12.13 | 11.77 | M7.0 | ... | ... | ... | ... | 4.5 ± 0.5 | (k) |
| SDSS162718.20+353835.7 | 17.56 | 12.35 | 11.73 | 11.35 | M7.0 | ... | ... | ... | ... | 8.0 ± 0.5 | (k) |
| SDSS220334.10+130839.8 | ... | 14.38 | 13.87 | 13.55 | M7.0 | ... | ... | ... | ... | ≤ 3.5 | (k) |
| SDSS225228.50 − 101910.9 | ... | 14.78 | 14.22 | 14.01 | M7.0 | ... | ... | ... | ... | ≤ 3.5 | (k) |
| TVLM513−46546 | ... | 11.87 | 11.18 | 10.71 | M9.0 | ... | ... | ... | ... | 60.0 | (f) |

**Table 3**
(Continued)

| Star | $V$ | $J$ | $H$ | $K_s$ | Spec Type | $T_{EFF}$ (K) | $\pi$ (mas) | $M/M_\odot$ | [Fe/H] | $v \sin i$ (km s$^{-1}$) | Source |
|---|---|---|---|---|---|---|---|---|---|---|---|
| TVLM868−110639 | ... | 12.61 | 11.84 | 11.35 | M9.0 | ... | ... | ... | ... | 30.0 | (f) |
| VB8 | 16.70 | 9.78 | 9.20 | 8.82 | M7.0 | 2425 | ... | ... | ... | 9.0 | (f) |
| VB10 | 17.30 | 9.91 | 9.23 | 8.77 | M8.0 | ... | ... | ... | ... | 6.5 | (f) |
| YZCMi | ... | ... | ... | ... | M5.5 | ... | ... | ... | ... | 5.3 | (j) |

**Notes.** Column 12 shows the source of each $v \sin i$ from the literature with references as follows: (a) Stauffer & Hartmann (1986); (b) Marcy & Chen (1992); (c) Delfosse et al. (1998); (d) Glebocki & Stawikowski (2000); (e) Gizis et al. (2002); (f) Mohanty & Basri (2003); (g) Bailer-Jones (2004); (h) Fuhrmeister & Schmitt (2004); (i) Jones et al. (2005); (j) Reiners (2007); (k) West & Basri (2009). Columns are the same as Table 1 except without the telluric widths in Column 15.

**Table 4**
M dwarf Activity Saturation Limits

| Spectral Type | $v \sin i$ (km s$^{-1}$) | $l$ (Gyr) |
|---|---|---|
| M4 | 8 | 5 |
| M5 | 10 | 7 |
| M6 | 12 | 7 |
| M7 | 13 | 8 |

The solid line connects the points and visually highlights the increasing trend toward later spectral types. Reid et al. (2002) suggest a flat distribution of rotation rates between stars of M6 and M9, whereas larger samples indicate this may not be the case (Mohanty et al. 2002; Reiners & Basri 2008). The medians indicate a rising trend through the mid-to-late M dwarfs, flattening off toward the end. Due to the change in distributions at the fully convective boundary, we perform two straightline fits to the medians in the spectral ranges M0–M3.5 and M4–M9. The best fit to the early M stars clearly shows a flat trend across the whole regime, whereas the fit to the late Ms shows a rising trend, appearing to flatten toward the later M stars (note the curvature due to logarithmic plotting). The fits to the early and late M star samples are described by $v \sin i = 0.09(\pm 0.30) \times \mathrm{SpT} + 3.41(\pm 0.67)$ km s$^{-1}$ and $v \sin i = 2.10(\pm 0.53) \times \mathrm{SpT} - 4.54(\pm 3.56)$ km s$^{-1}$, with standard uncertainties, represented by the dotted lines in the plot, of $\pm 0.89$ km s$^{-1}$ and $\pm 2.79$ km s$^{-1}$, respectively. The total sample of less than 300 is still rather small, especially when binned. Indeed there appears a dearth of objects between M6.5 and M8.5 with rotation rates above $\sim$15 km s$^{-1}$, which may indicate another population change above M6.5. The evidence for this gap is weak at present due to the low number of stars in these spectral bins; therefore, further observations are needed and any biases studied to fully validate the existence of this feature.

At temperatures below around 2800 K (approximately M6–M7-type objects) dust formation and opacity are important in stellar/substellar atmospheres (Tsuji et al. 1996; Jones & Tsuji 1997; Tinney et al. 1998; Chabrier et al. 2000; Baraffe et al. 2002 and references therein). Berger et al. (2008) have shown that late-M stars mark a transition in the properties of the magnetic field and its dissipation, along with high temperature plasma being generated in the outer atmosphere. They go on to hypothesize that the stellar rotation may play a part in this process, and indeed the difference shown here between the mid- and late-type M stars seems to add to this conclusion. A KS test reveals a $D$-statistic of 0.639, or $5.413 \times 10^{-6}$%, that stars in the range M0.0–M6.5 and those in the range M7.0–M9.5 are drawn from the same parent distribution. However, given that we have already shown there to be a large difference between early Ms (M0–M3.5), this will bias this probability test. When we remove all stars

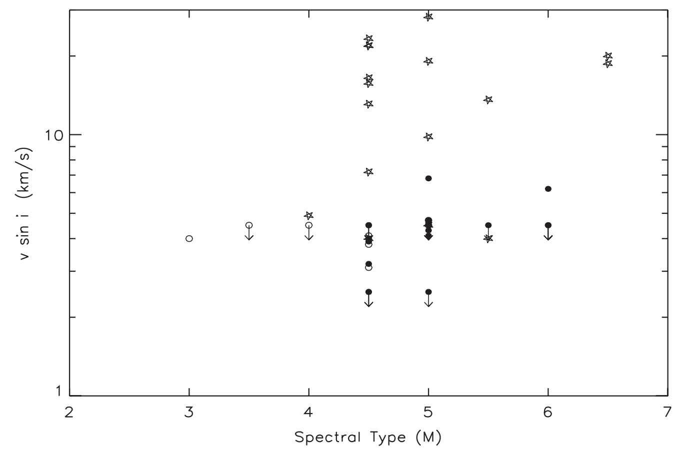


**Figure 10.** Distribution of rotational velocities against spectral type for stars in this study with a split based on each star's H$\alpha$ profile. The filled circles represent stars with no significant H$\alpha$ emission or absorption. The open circles are stars with significant H$\alpha$ absorption and the stars represent objects with detected H$\alpha$ emission. All stars with velocities greater than 7 km s$^{-1}$ have detected H$\alpha$ emission. Also no significant H$\alpha$ absorption was detected in stars later than M5.

earlier than M4, we find a $D$-statistic of 0.544, which relates to a probability of only $1.437 \times 10^{-3}$% that these are drawn from the same parent population. This $>5\sigma$ result may indicate that at temperatures when dust opacity becomes important there is a change in the rotational braking mechanisms and hence the magnetic properties of ultracool dwarfs. This might give rise to the flattening trend indicated between M6.5 and M9 stars; however, a more comprehensive study is needed, particularly to decouple the age of these stars by studying the space motion to determine if they are young or old disk stars. Also the biases of the literature surveys are important. For instance, studies like those of West & Basri (2009) focus only on selecting inactive, and hence slowly rotating, late-type M stars. In addition, current models show that the late M star regime can also be populated by young brown dwarfs. Finally, this relation also suffers from the lack of low $v \sin i$ detections already mentioned above, even more so given the M6.5 detection boundary. Therefore, we expect this result might also become more pronounced with further low $v \sin i$ detections at spectral types below M6.5.

The normalized distribution of $v \sin i$ values is represented by the histograms in Figure 11, where the solid histogram is for all stars in the spectral range between M0 and M3.5, and the dashed histogram is for all stars in the range M4–M9.5. These include all values determined in this work combined with those in the literature. It is apparent that both distributions peak at low rotation rates ($\sim$3 km s$^{-1}$), with peak values of 55 and 42 stars, respectively. We find that the total number of $v \sin i$'s $\leqslant$ 10 km s$^{-1}$ is 198, and these should represent useful stars

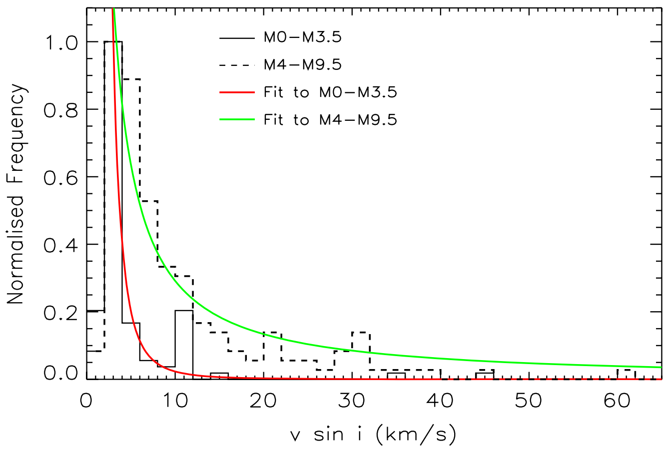


**Figure 11.** Histograms of rotation velocities in this sample and in the literature split by spectral type. The solid curve represents the stars in the spectral range from M0 to M3.5, whereas the dashed curve represents the stars between M4 and M9.5. Both samples peak at low rotation velocities of around ~3 km s$^{-1}$; however, the bins that contain the later type objects have many more stars with measurable $v$ sin $i$. The solid curves are the best-fit power laws to the data, with the red (dark gray) curve representing the M0–M3.5 bins and the green (light gray) curve representing the M4–M9.5 data. The changing power law between the two spectral regions highlights a possible change in the rotational distribution for fully convective stars.

(A color version of this figure is available in the online journal.)

for future near-infrared radial-velocity planet search projects such as PRVS. Bouchy et al. (2001) show that the information content drops by a factor of ~3.5 between rotation velocities of ~2–10 km s$^{-1}$, making $\geqslant$ 10 km s$^{-1}$ a reasonable M star radial-velocity selection cut. This sample is still large (124) when we include all mid-to-late M stars in the range M3–M9.5 (stars where obtaining optical precision radial velocities becomes extremely difficult). Note the binary systems have been left out of Figures 11 and 9 since the combined luminosities will generate inaccurate photometry and therefore inaccurate spectral types. Also, binary systems like these make radial-velocity exoplanet searches much harder since any small planetary signature is masked by the large short-period binary velocity, meaning these are not ideal planet search targets for precision radial-velocity programs moving into an unexplored parameter space.

Comparing the distributions of both histograms helps to probe the possible changing rotational properties of M stars at the fully convective boundary. We have employed two power-law fits to each distribution separately in order to test the changing velocity distribution between these two regimes. The red (dark gray)[6] curve is fit to the sample of early M dwarfs between M0 and M3.5, whereas the green (light gray) curve is fit to the mid-to-late M dwarf sample. The fits are made to the bins by including Poisson uncertainties which are not shown in the plot for clarity. It can be seen that the fit to the early M stars drops much more rapidly than the fit to the later Ms. The power laws are described by $\delta N/\delta v \sin i \propto x^{-3.13}$ for the early Ms, whereas for the later Ms it is only found to be $\propto x^{-1.12}$, highlighting the differing steepness of each slope. The early Ms have a much longer tail than the later Ms due to this faster decay of the distribution, and this is also probably an underestimate since we included all upper limits in the data to increase the sample size, which included a number of stars from the Stauffer & Hartmann (1986) sample with detection limits of 10 km s$^{-1}$. We note that the curvature of these slopes is also affected by the activity lifetimes shown in Table 4 since they change with spectral type.

The difference of 2.01 in the exponent between the two spectral samples allows us an insight into the efficiency of the braking mechanism between partially and fully convective stars, assuming the larger measured rotation in the later M star sample is not due to increased line blending from increased molecular bands and instrumental resolution arguments. Delfosse et al. (1998) have shown that the majority of rapidly rotating mid-M stars are members of the young disk population, whereas the older population tend to rotate more slowly. If this is indeed the case, then the braking mechanism is at play in later M stars, but the efficiency has dropped across the fully convective boundary. As mentioned earlier, the change in the field topology between the partially and fully convective boundary is probably the driving factor which governs the efficiency of the wind-braking mechanism since Reiners & Basri (2007) have shown that fully convective stars produce field strengths as strong as partially convective stars. To better probe the braking mechanism in this fashion, in addition to gaining more data, it is necessary to also fold in an age proxy for the sample, and decouple both the young and old disk populations to compare these objects. Along with this a better understanding of the activity lifetimes and how these change with spectral type should be considered. More magnetic field topology studies are required for later M stars which can help to confirm if the later Ms also have axisymmetric poloidal fields and add weight to the topology argument. Finally, more detailed testing of changes around the dusty regime (~M6.5) where stars can also be young brown dwarfs might usefully be investigated.

## 6. CONCLUSIONS

We present the initial results from our study of rotation rates for a range of M stars as part of our target selection for a PRVS-like planet search project. We observed over 50 M stars with HRS on the HET with the aim of selecting the slowest rotators in order that a near infrared planet search survey, such as PRVS, shall have a statistically large sample of M stars where highly precise radial-velocity measurements can be accrued. Of our sample of 49 suspected single M stars between M3 and M6.5, we find 36 have $v$ sin $i$ values $\leqslant$ 10 km s$^{-1}$ which will represent good radial-velocity targets. When we include all literature M stars in the optically difficult radial-velocity regime (M3–M9.5) we find this value increases to 124.

We also confirm the increase of rotational velocities between early to mid M stars. This change at the fully convective boundary seems to be linked to a change in the topology of the magnetic fields between such stars, indicating axisymmetric poloidal fields drive a less efficient wind-braking mechanism. Also there is an initial indication that stars with spectral types in the range M6.5–M8.5 have a different rotational velocity distribution compared with those of below M6.5, as the distribution appears to flatten off beyond this regime. Since this is around the temperature where dust opacity becomes important (~2800 K), there may be another change in the efficiency of the braking mechanism in such stars which could indicate another magnetic field topology change. In addition, we also show how knowledge of the $v$ sin $i$ can be used to put a lower, or upper, limit on the age of mid-M dwarf stars, since the rotation-activity relation has a temperature dependent saturation level.

[6] The colors in the brackets relate to the printed document, whereas the colors in the text are for the online edition of the article.

We also highlight the rotation-activity relation through emission, or lack thereof, of the H$\alpha$ line. There appears a boundary of around 7 km s$^{-1}$ between stars with and without H$\alpha$ emission, with the fast rotators almost always exhibiting such emission, however since the sin $i$ degeneracy is present it is difficult to account for any firm empirical boundaries with small numbers. We observed the star GJ1253 over two epochs and found the H$\alpha$ emission had switched on over a period of less than one month. This may be due to an active region rotating in and out of our field of view with a period equal to the rotation period of the star, or due to a flaring event.

We have also discovered three spectroscopic binary systems and confirmed another. Both components in the GJ1080 system produce fairly similar profiles, indicating they are of similar spectral type, the secondary likely a little cooler and less luminous. The profiles for GJ3129 and Gl802 are widely separated and both of these exhibit double H$\alpha$ emission features. Gl802 is also a known triple system, but we find evidence for another companion in the system; however, given the noise due to blended light from at least three separate sources the evidence is weak. In comparison to these fairly strong profiles, the secondary profile in the LHS3080 system is significantly weaker, indicating the companion is significantly cooler than its host star. Finally, we have flagged other M dwarfs where there is some evidence for binary companions in these systems.

J.S.J. acknowledges partial support from Centro de Astrofísica FONDAP 15010003, along with partial support from GEMINI-CONICYT FUND and partial support from Comité Mixto ESO-GOBIERNO DE CHILE. This work also used the research computing facilities at the Centre for Astrophysics Research, University of Hertfordshire. Y.P.'s work was partially supported by the Microcosmophysics program of National Academy of Sciences and National Space Agency of Ukraine. The Hobby–Eberly Telescope (HET) is a joint project of the University of Texas at Austin, the Pennsylvania State University, Stanford University, Ludwig-Maximilians-Universität München, and Georg-August-Universität Göttingen. The HET is named in honor of its principal benefactors, William P. Hobby and Robert E. Eberly. Our research has made use of the SIMBAD database operated at CDS, Strasbourg, France. We also acknowledge the very helpful comments from the anonymous referee.

## REFERENCES


Bailer-Jones, C. A. L. 2004, A&A, 419, 703
Baraffe, I., Chabrier, G., Allard, F., & Hauschildt, P. H. 2002, A&A, 382, 563
Barnes, J. R., Collier Cameron, A., Unruh, Y. C., Donati, J. F., & Hussain, G. A. J. 1998, MNRAS, 299, 904
Berger, E., et al. 2008, ApJ, 676, 1307
Bonfils, X., et al. 2005, A&A, 442, 635
Bouchy, F., Pepe, F., & Queloz, D. 2001, A&A, 374, 733
Bouchy, F., et al. 2005, A&A, 444, L15
Butler, R. P., et al. 2006, ApJ, 646, 505
Byrne, P. B., Eibe, M. T., & Rolleston, W. R. J. 1996, A&A, 311, 651
Carpenter, J. M. 2001, AJ, 121, 2851
Casagrande, L., Flynn, C., & Bessell, M. 2008, MNRAS, 389, 585
Chabrier, G., Baraffe, I., Allard, F., & Hauschildt, P. 2000, ApJ, 542, 464
Collier Cameron, A., Horne, K., Penny, A., & Leigh, C. 2002, MNRAS, 330, 187
Delfosse, X., Forveille, T., Perrier, C., & Mayor, M. 1998, A&A, 331, 581
Delfosse, X., et al. 2000, A&A, 364, 217
Donati, J.-F., & Collier Cameron, A. 1997, MNRAS, 291, 1
Donati, J.-F., et al. 2008, MNRAS, 390, 545
Fleming, T. A., Giampapa, M. S., & Schmitt, J. H. M. M. 2000, ApJ, 533, 372
Fuhrmeister, B., & Schmitt, J. H. M. M. 2004, A&A, 420, 1079
Gizis, J. E., Reid, I. N., & Hawley, S. L. 2002, AJ, 123, 3356
Glebocki, R., & Stawikowski, A. 2000, Acta Aston., 50, 509
Gray, D. F. (ed.) 1992, The Observation and Analysis of Stellar Photospheres. (Cambridge Astrophysics Series, Vol. 20; Cambridge: Cambridge Univ. Press)
Henry, G. W., Donahue, R. A., & Baliunas, S. L. 2002, ApJ, 577, L111
Henry, T. J., et al. 2006, AJ, 132, 2360
Horne, K. 1986, PASP, 98, 609
Ireland, M. J., Kraus, A., Martinache, F., Lloyd, J. P., & Tuthill, P. G. 2008, ApJ, 678, 463
Jenkins, J. S., et al. 2008, A&A, 485, 571
Johnson, J., & Apps, K. 2009, ApJ, 699, 933
Jones, H. R. A., & Tsuji, T. 1997, ApJ, 480, L39
Jones, H. R. A., et al. 2005, MNRAS, 358, 105
Jones, H. R. A., et al. 2008, Proc. SPIE, 7014, 31
Kupka, F., & Ryabchikova, T. A. 1999, in Proc. 12th Natl Conf. of Yugoslav Astronomers and International Workshop 65, Development of Astronomical Databases, ed. L. Č. Popović & M. DaČić (Belgrade: Publications de l'Observatoire Astronomique de Beograd), 223
Lee, K.-G., Berger, E., & Knapp, G. R. 2009, ApJ, submitted (arXiv:0905.3182)
Lloyd, J. P., et al. 2006, ApJ, 650, L131
Marcy, G. W., & Butler, R. P. 1992, PASP, 104, 270
Marcy, G. W., & Butler, R. P. 1996, Proc. SPIE, 2704, 46
Marcy, G. W., & Chen, G. H. 1992, ApJ, 390, 550
Markwardt, C. B. 2009, arXiv:0902.2850
Martín, E. L., & Ardila, D. R. 2001, AJ, 121, 2758
Mayor, M., et al. 2009, A&A, 493, 639
McCarthy, C., & Zuckerman, B. 2004, AJ, 127, 2871
Mills, D., Webb, J., & Clayton, M. 1996, Starlink, 152, 1
Mohanty, S., & Basri, G. 2003, ApJ, 583, 451
Mohanty, S., Basri, G., Shu, F., Allard, F., & Chabrier, G. 2002, ApJ, 571, 469
Morin, J., et al. 2008, MNRAS, 390, 567
Noyes, R. W., Hartmann, L. W., Baliunas, S. L., Duncan, D. K., & Vaughan, A. H. 1984, ApJ, 279, 763
Osten, R. A., Hawley, S. L., Allred, J. C., Johns-Krull, C. M., & Roark, C. 2005, ApJ, 621, 398
Patten, B. M., & Simon, T. 1996, ApJS, 106, 489
Pepe, F., et al. 2000, Proc. SPIE, 4008, 582
Pravdo, S. H., Shaklan, S. B., & Lloyd, J. 2005, ApJ, 630, 528
Ramsey, L. W., et al. 1998, Proc. SPIE, 3352, 34
Ramsey, L. W., et al. 2008, PASP, 120, 887
Reid, I. N., et al. 2002, AJ, 124, 519
Reiners, A. 2007, A&A, 467, 259
Reiners, A. 2009, A&A, 498, 853
Reiners, A., & Basri, G. 2007, ApJ, 656, 1121
Reiners, A., & Basri, G. 2008, ApJ, 684, 1390
Rivera, E. J., et al. 2005, ApJ, 634, 625
Rockenfeller, B., Bailer-Jones, C. A. L., & Mundt, R. 2006, A&A, 448, 1111
Skrutskie, M. F., et al. 2006, AJ, 131, 1163
Stauffer, J. R., & Hartmann, L. W. 1986, ApJS, 61, 531
Tinney, C. G., Delfosse, X., Forveille, T., & Allard, F. 1998, A&A, 338, 1066
Tsuji, T., Ohnaka, K., & Aoki, W. 1996, A&A, 305, L1
Tull, R. G. 1998, Proc. SPIE, 3355, 387
Udry, S., et al. 2007, A&A, 469, L43
van Altena, W. F., Lee, J. T., & Hoffleit, D. 1995, VizieR Online Data Catalog, 1174, 0
West, A. A., & Basri, G. 2009, ApJ, 693, 1283
West, A. A., Hawley, S. L., Bochanski, J. J., Covey, K. R., & Burgasser, A. J. 2009, in IAU Symp. 258, The Ages of Stars, ed. E. E. Mamajek, D. R. Soderblom, & R. F. G. Wyse (Dordrecht: Kluwer), 327
Wright, J. T. 2005, PASP, 117, 657